Anatomy of the high-frequency ambient seismic wave field at the TCDP borehole

G. Hillers,[1] M. Campillo,[1] Y.-Y. Lin,[2] K.-F. Ma,[2] and P. Roux[1]

Received 4 November 2011; revised 19 April 2012; accepted 20 April 2012; published 1 June 2012.

[1] The Taiwan Chelungpu-fault Drilling Project (TCDP) installed a vertical seismic array between 950 and 1270 m depth in an active thrust fault environment. In this paper we analyze continuous noise records of the TCDP array between 1 and 16 Hz. We apply multiple array processing and noise correlation techniques to study the noise source process, properties of the propagation medium, and the ambient seismic wave field. Diurnal amplitude and slowness patterns suggest that noise is generated by cultural activity. The vicinity of the recording site to the excitation region, indicated by a narrow azimuthal distribution of propagation directions, leads to a predominant ballistic propagation regime. This is evident from the compatibility of the data with an incident plane wave model, polarized direct arrivals of noise correlation functions, and the asymmetric arrival shape. Evidence for contributions from scattering comes from equilibrated earthquake coda energy ratios, the frequency dependent randomization of propagation directions, and the existence of correlation coda waves. We conclude that the ballistic and scattered propagation regime coexist, where the first regime dominates the records, but the second is weaker yet not negligible. Consequently, the wave field is not equipartitioned. Correlation signal-to-noise ratios indicate a frequency dependent noise intensity. Iterations of the correlation procedure enhance the signature of the scattered regime. Discrepancies between phase velocities estimated from correlation functions and in-situ measurements are associated with the array geometry and its relative orientation to the predominant energy flux. The stability of correlation functions suggests their applicability in future monitoring efforts.

Citation: Hillers, G., M. Campillo, Y.-Y. Lin, K.-F. Ma, and P. Roux (2012), Anatomy of the high-frequency ambient seismic wave field at the TCDP borehole, *J. Geophys. Res.*, *117*, B06301, doi:10.1029/2011JB008999.

1. Introduction

[2] Deep boreholes allow direct observations of fault zone structure. Equipped with downhole sensors, such boreholes on the kilometer scale provide additional excellent seismological data to study properties of earthquake sources [*Abercrombie*, 1995] and of the propagation medium [*Chavarria et al.*, 2004; *Malin et al.*, 2006; *Bohnhoff and Zoback*, 2010] due to significantly reduced noise levels. For example the San Andreas Fault Observatory at Depth (SAFOD) has led to pioneering observations associated with the structure and dynamics of an active strike-slip fault segment [*Zoback et al.*, 2011].

[3] The Taiwan Chelungpu-fault Drilling Project (TCDP) (hole A) constitutes a similar natural fault zone laboratory in an active thrust fault environment (Figure 1a). The borehole perforates the slip zone of the 1999 M7.6 Chi-Chi earthquake at 1111 m depth. Geophysical logging and coring, and a hydraulic cross-hole experiment reveal a complex crustal and fault zone architecture and associated hydro-mechanical properties [*Doan et al.*, 2006; *Wu et al.*, 2007]. Signals recorded around 1100 m depth have been analyzed to study seismicity, structure, and physical properties of the Chelungpu fault [*Wang et al.*, 2012], source scaling of microearthquakes [*Lin et al.*, 2012], and fault zone dynamics (K.-F. Ma et al., Evidence on isotropic events observed with a borehole array in the Chelungpu Fault Zone, Taiwan, submitted to *Science*, 2012).

[4] Seismic arrays, in general, facilitate the analysis of directional and compositional properties of ballistic [e.g., *Rost and Thomas*, 2002, and references therein] and scattered [e.g., *Hennino et al.*, 2001; *Koch and Stammler*, 2003; *Roux et al.*, 2005; *Koper et al.*, 2009; *Margerin et al.*, 2009] wave fields. Downhole arrays, in particular, are superior to

[1]Institut des Sciences de la Terre, Université Joseph Fourier, CNRS, Grenoble, France.
[2]Department of Earth Sciences and Institute of Geophysics, National Central University, Jhongli, Taiwan.

Corresponding author: G. Hillers, Institut des Sciences de la Terre, Université Joseph Fourier, CNRS, FR-38041 Grenoble, France. (hillersg@ujf-grenoble.fr)

0148-0227/12/2011JB008999

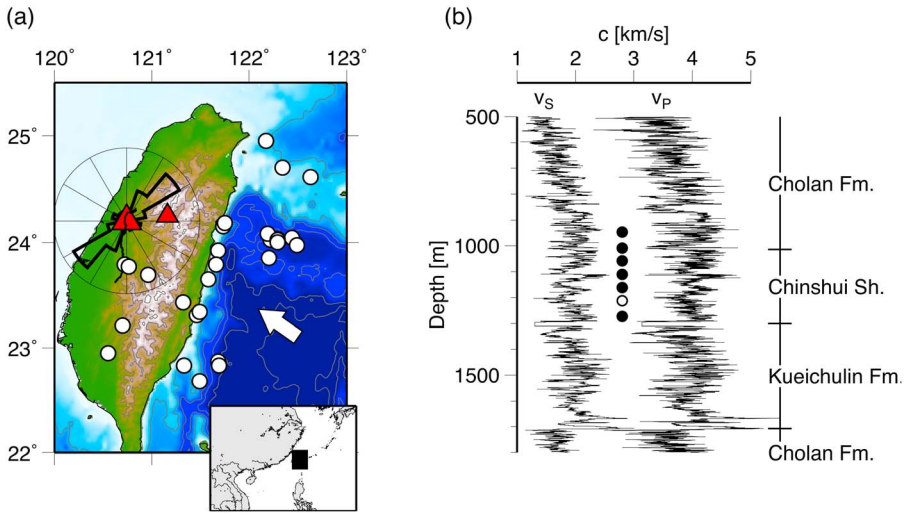

Figure 1. (a) The map illustrates the geographical situation of the study area. The large and small triangle denote the TCDP site and the surface broadband station TDCB, respectively. The Chelungpu fault is indicated by the North-South trending black line. The arrow indicates the vector of relative motion between the Philippine Sea plate and the Eurasian plate [*Wu et al.*, 2007]. White circles show hypocenters of 35 regional earthquakes used in the H^2/V^2 (section 3.2) and polarization analysis (Appendix D) (some hypocenters are outside the map boundaries). The rose diagram centered at the TCDP location shows azimuth estimates of the (coherent) noise propagation direction (section 4.1; data as in Figure 6d). (b) Depth profiles of in-situ phase velocities v_P and v_S [*Wu et al.*, 2007]. Data are sampled in 0.125 m intervals. Phase velocities across the array depth range are $v_P = 4 \pm 0.3$ km/s and $v_S = 2 \pm 0.2$ km/s, respectively. Dots mark the position of the seven TCDP borehole sensors, labeled BHS1–7 from top to bottom. BHS6 is not used in the analysis. The legend to the right indicates geologic layers [*Wu et al.*, 2007]. 'Fm.' and 'Sh.' abbreviate 'formation' and 'shale', respectively.

antennas located at the surface due to an enhanced phase coherence at depth that results from the shielding of rapidly attenuating surface wave noise. Focusing on scattered wave fields, continuous borehole array recordings provide a valuable resource to study the constituents of the ambient seismic or 'noise' wave field, to investigate potentially competing noise source processes that act at different spatial and temporal scales, and to draw conclusions about randomization and propagation effects of the medium. In this study, we research source and medium properties associated with the high-frequency (>1 Hz) ambient wave field recorded by the TCDP downhole array.

[5] Source processes that excite noise at these frequencies include anthropogenic activities [*Ringdal and Bungum*, 1977; *Gurrola et al.*, 1990; *Young et al.*, 1996; *Atef et al.*, 2009; *Lewis and Gerstoft*, 2012], wind acting on topographic irregularities [*Withers et al.*, 1996; *Hillers and Ben-Zion*, 2011], precipitation and runoff [*Burtin et al.*, 2008], and thermoelastic straining [*Berger*, 1975; *Ben-Zion and Leary*, 1986; *Hillers and Ben-Zion*, 2011]. Scattering and attenuation properties of the crustal material control the randomization of energy propagation directions and relative mode excitation [*Margerin et al.*, 1998, 2001; *Larose et al.*, 2008]. Together, the spatio-temporal distribution and excitation properties of noise sources and the scattering properties of the medium control the characteristics of the ambient wave field.

[6] The diffuse wave field associated with scattering approaches—at long lapse times with respect to the pulse-source event—equipartition [*Campillo and Paul*, 2003; *Paul et al.*, 2005]. In this asymptotic regime all possible modes are randomly excited with equal weight on average [e.g., *Campillo*, 2006, and references therein], and energy ratio markers are equilibrated. In contrast to pulse-sources, continuously acting sources can also lead to a stabilization of energy markers. In that case, stabilization is associated with the source process, and the propagation regime will not approach equipartition; consequently diffuse and ballistic energy propagation coexist, where the relative contributions depend on the source-receiver distance, source intensity, and scattering and attenuation properties of the medium.

[7] Our TCDP high-frequency noise analysis thus targets the assessment of diffuse and ballistic components. The discussion of source, medium, and wave field properties includes amplitude patterns (section 3.1); estimates of the direction of energy flow (sections 3.3 and 4.1); stabilization properties of the kinetic noise energy ratio H^2/V^2 (section 3.2); the coherence evolution and properties of the direct arrival and the coda of noise correlation functions (sections 4 and 5).

[8] The analysis reveals a complex anatomy of the ambient seismic wave field at 1 km depth. Key observations include diurnal amplitude and slowness variations, time asymmetric correlation functions, narrow azimuthal distributions of predominantly upward coherent energy flux, and generally stabilized kinetic energy ratios. Together, these observations suggest continuously acting, anisotropic cultural sources, and a partial randomization by the medium of the excited wave field. This leads to a coexistence of the ballistic and diffuse propagation regime, with the first regime dominating the records.

Table 1. A Summary of Measurements Inferred With Different Analysis Techniques[a]

	f_c [Hz]			
	1.5	3	6	12
Beamforming				
s [s/km], Z-component	0.06	0.20	0.19	−0.02
ϕ [°] with v_P = 4 km/s	76	37	41	95
s [s/km], N-component	0.11	0.31	0.40	0.11
ϕ [°] with v_S = 2 km/s	77	52	37	77
s [s/km], E-component	0.08	0.30	0.29	−0.41
ϕ [°] with v_S = 2 km/s	80	53	55	145
Polarization Analysis				
Incidence ϕ [°]	25	27	24	26
Azimuth θ [°]	61	43	77	79
Rectilinearity R	0.99	1.00	0.99	0.93
C^1 Direct Arrival Phase Velocities ($dz \geq \lambda/5$)[b]				
c [km/s], from ZZ-C^1			4.4	
c [km/s], from NN-C^1		3.6	2.7	
c [km/s], from EE-C^1		3.6	2.8	
C^3 Direct Arrival Phase Velocities ($dz \geq \lambda/5$)[b]				
c [km/s], from ZZ-C^{3-}			4.0	
c [km/s], from ZZ-C^{3+}			4.2	

[a]All values are medians from the temporal analysis (beamforming), or from inter-sensor correlation pairs.

[b]Here the $dz \geq \lambda/5$ criterion prevents any measurement in the f_c = 1.5 Hz band and estimates in the f_c = 3 Hz band associated with P-waves. For the f_c = 12 Hz band, the SNR is not sufficient.

[9] The organization of the paper follows the application of analysis techniques. Detailed discussions on technical aspects can be found in the appendices. Implications of the individual results—which are summarized in Table 1—are discussed in the corresponding sections and synthesized in the concluding section. Throughout the analysis, we consider the utilization of the wave field and derived correlation functions in future noise-based monitoring studies [*Courtland*, 2008]. Beginning with section 3.2, the analysis is divided into four frequency bands centered at f_c = 1.5, 3, 6, 12 Hz, with corresponding bandwidths Δf = 1, 2, 4, 8 Hz. This leads to the contextual discrimination between low, intermediate, and high frequencies. During parts of our analysis, we separate data recorded during day- and night-time hours. In this context, '24-h' refers to analyses where this distinction is not made.

2. Recording Environment and Data

[10] The TCDP (hole A) site is located in the town of Dakeng, about 2 km east of the Chelungpu fault surface trace at an elevation of 245 m [*Wu et al.*, 2007] (Figure 1a). The site is situated in a mountainous environment, yet close to the densely populated lowlands of western Taiwan. The Chelungpu fault dips 30° east, and the 1.8 km deep borehole pierces the slip zone of the M7.6 1999 Chi-Chi earthquake at 1111 m depth [*Ma et al.*, 2006]. The convergence of the Philippine Sea plate with respect to the Eurasian plate at a rate of 82 mm/yr results in one of the most active plate boundaries characterized by ongoing orogenesis and high seismic activity [*Wang et al.*, 2010].

[11] Seven short period, 4.5 Hz natural frequency, Galperin 3-component (N, E, Z) velocity seismometers are located between 946 m and 1274 m depth below the surface, with an average 50-meter spacing (Figure 1b). The top three sensors (BHS1–BHS3) are located in the hanging wall. The central sensor (BHS4) is placed near the 1999 slip zone, and the remaining three sensors (BHS5–BHS7) are placed in the foot wall [*Wang et al.*, 2012]. Velocity logs indicate average compressional and shear velocities of $v_P = 4.0 \pm 0.3$ km/s and $v_S = 2.0 \pm 0.2$ km/s across the array (Figure 1b). Intermittent steep gradients in the velocity profiles between 500 m and ~1900 m depth correspond to abrupt stress orientation changes associated with lithologic boundaries and/or logged faults [*Wu et al.*, 2007]. Low Q values between the slip zone and sensor BHS1 compared to Q below BHS4 suggests overall damaged and compliant material in the hanging wall [*Wang et al.*, 2012]. Three major fault zones with dip angles between 30° and 45° east have been identified between 1100 and 1250 m [*Hirono et al.*, 2007]. Reduced velocities are observed, however, only on the meter scale around these primary deformation carriers. This is in contrast to the extended fault-parallel low-velocity zone characteristic for strike-slip faulting environments [*Ben-Zion*, 2008].

[12] We analyze continuous data recorded in 2008 and 2009, focusing on about 15 days in early 2009. The original sampling rate is 200 Hz. Sensor BHS6 is not considered in this study due to persistent recording problems. No collocated surface sensor exists during this time period. To compare borehole observables with surface measurements, we use data from the closest available broadband station, a 47-kilometer distant STS-1 seismometer, TDCB (Figure 1a). Heterogeneous cementation along the casing causes coupling problems [*Doan et al.*, 2006]. No detailed coupling log exists that can be used for reconciliation.

3. The Ambient Seismic Wave Field

[13] We begin the analysis by investigating fundamental properties of the ambient wave field, i.e., frequency, time, and space dependent amplitude distributions (section 3.1), the propagation regime (section 3.2), and propagation directions (section 3.3). We show that amplitude patterns allow conclusions about the source process, that the energy propagation regime is controlled by source and medium properties, and that flux direction estimates are associated with the source distribution.

3.1. Spectral Amplitudes

[14] High-resolution spectrograms (Figure 2a) are obtained by computing the amplitude spectrum of consecutive, non-overlapping, tapered 5 min windows. Predominant diurnal amplitude variations between 1 and 20 Hz are associated with cultural activity. Amplitudes differ by a factor of 2–4 between day- and night-time hours, and day-time amplitudes during Sundays are reduced with respect to working days. The anthropogenic source process controls the amplitude pattern for frequencies up to 80 Hz, as revealed by the spectral analysis of a continuous, 60 days long amplitude time series sampled at 1/minute. In contrast to frequencies below 40 Hz, night-time amplitudes exceed day-time amplitudes at these very high frequencies.

[15] To construct estimates of daily amplitude distributions (Figure 2b), we first compute the amplitude spectrum of consecutive, non-overlapping 5 min windows. The resulting 288 amplitude values at each frequency constitute the frequency dependent amplitude density distribution [*McNamara*

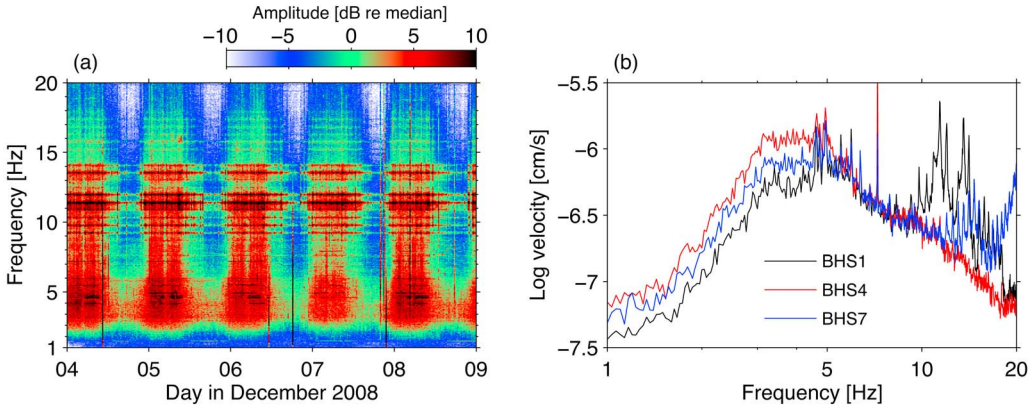

Figure 2. (a) The vertical component spectral amplitude distribution is dominated by a diurnal pattern. Time is GMT. December 7—showing lower amplitudes compared to other days—is a Sunday. Data are from the top sensor, BHS1. Data are scaled by the median value of the shown total 2-dimensional data set. (b) The spectra show vertical-component, day-time low-noise levels from the top (black), center (red), and lowest (blue) sensors. Key features of the amplitude-frequency pattern is the depth dependence of the noise level below 5 Hz, spurious peaks associated with electronic noise above 5 Hz, and a peak between 6 and 7 Hz associated with an industrial source.

and Buland, 2004]. From this, we define the 0.025-quantile level as the daily low-noise level, considering that the zero-quantiles are occasionally corrupted by intermittent recording problems.

[16] The shape of the spectral distribution is characterized by an increase between 1 and 3 Hz, a relatively flat portion between 3 and 6 Hz, and a decay towards larger frequencies modulated by a series of narrow peaks (Figure 2b). The rising low-frequency noise level is a consequence of the instrument response characteristics. The flat part is situated around the natural frequency of 4.5 Hz. Some sensors and components exhibit one or two broader peaks at frequencies larger than 10 Hz (black and blue lines in Figure 2b). The position of these peaks varies between sensors. We attribute these signals to resonance effects associated with the dipping layers. A comprehensive analysis requires detailed modeling of relevant wave propagation effects which is beyond the scope of this paper.

[17] In addition to these broad peaks, a series of narrow spectral lines at frequencies >5 Hz spaced at about 0.55 Hz appears in spectrograms on all components and sensors. We considered several causative mechanisms, among others 'F-type' events (Ma et al., submitted manuscript, 2012), resonance of fluid filled cracks [*Ferrazzini and Aki*, 1987; *Chouet*, 1988; *Bohnhoff and Zoback*, 2010], and coupling phases. They were, however, collectively rejected based on incompatibilities with the properties of the spectral peaks. The evenly spaced peaks are manifestations of electronic noise. They are spurious tones from the analog-to-digital converter associated with a leakage effect of the reference timing signal. It indicates that the seismic noise amplitude level interferes with the electronic noise level. The narrow peaks are completely removed when spectral estimates are smoothed with a logarithmic window [*Konno and Ohmachi*, 1998], testament to their infinitesimal bandwidth, which further corroborates their spurious character.

[18] This affects analyses that are sensitive to amplitudes of the wave field, e.g., the H^2/V^2 estimates discussed in section 3.2. The 24-hour periodicity at frequencies up to 80 Hz is not biased by this phenomenon; narrow frequency bands that in- and exclude spurious peaks show the same trend. Results obtained with processing techniques that focus on phase characteristics of the wave field are also not influenced by this artifact.

[19] Vertical component noise has consistently lower amplitudes compared to horizontal amplitudes up to about 10 Hz; at higher frequencies, this pattern is inverted. The noise level at the 40-kilometer distant surface station TDCB is larger compared to borehole amplitudes. This is compatible with the general observation that high-frequency noise attenuates with depth [e.g., *Young et al.*, 1996]. At 3–6 Hz, however, the borehole low-noise level exceeds the surface low-noise level during day-time hours. This can be explained by the peak sensor sensitivity at these frequencies and the closer vicinity of the downhole array to cultural activity. At frequencies up to 6 Hz the topmost sensor BHS1 shows the smallest amplitudes, followed by the deepest sensor BHS7. The largest amplitudes are measured at the center station, BHS4, which further suggests the relevance of resonance. The generally depth-inverted amplitude pattern indicates a predominantly upward propagation of energy, a hypothesis that will be substantiated below.

[20] We study daily low-noise levels over the two-year observation period (Figure 3a) to select a time window that is not affected by possible transients. The pattern suggests a seasonal dependence, because increased relative amplitudes occur mainly during the monsoon season in summer. We limit the analysis of seasonal signals in the TCDP data set to a visual comparison of the spectral amplitude patterns and time series of precipitation and wind speed. We find an overall better agreement between low-noise levels and strong precipitation events and associated amplified runoff (Figure 3b) in the Dakeng stream passing the TCDP site at 300 m distance. Some large amplitude episodes also coincide with increased wind speeds (Figure 3c). Records of wind direction, atmospheric pressure, and temperature do not suggest a causal relationship with the high-frequency low-noise level at depth. We conclude that data recorded during Northern Hemispheric winter

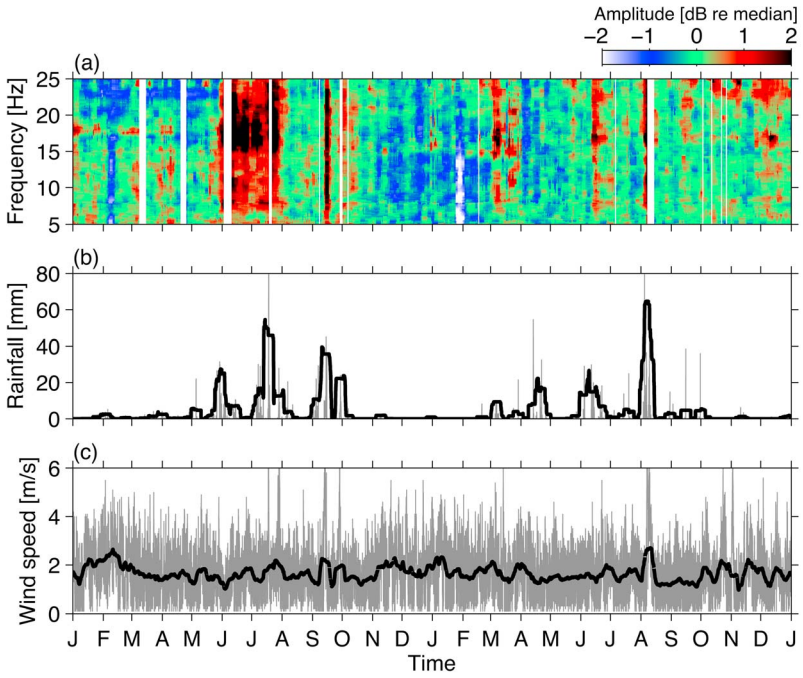

Figure 3. (a) Daily low-noise amplitude estimates, (b) rainfall and (c) wind speed data from 2008 and 2009. Data in Figure 3a are smoothed with a 7-point temporal and 15-point frequency median filter. Each frequency bin is scaled by its temporal median. Grey lines in Figures 3b and 3c show hourly sampled data, and black lines are 10-day moving averages (upscaled in Figure 3b to appear as envelope). Meteorological data are collected about 10 km west of the TCDP site.

months are least affected by natural events. Therefore—and because of a more complete data set in 2009—we will utilize continuous data from early 2009 to analyze typical properties of the high-frequency ambient seismic wave field.

[21] We emphasize that precipitation events do not leave a footprint in spectrograms of consecutive time windows on a sub-hour scale as in Figure 2a; only daily low-noise levels show a dependence on precipitation pattern. Seasonal fluctuations of the noise level are hence smaller compared to diurnal changes associated with anthropogenic activity.

[22] To summarize, relatively large amplitudes at depth compared to distant surface measurements imply a closer vicinity of the borehole site to the source. The frequency-dependent amplitude pattern across the downhole array (relative horizontal to vertical and day- vs. night-time amplitudes) results from a combination of time dependent excitation and space dependent properties of the stratified medium. Further effects of the medium on the wave field constituents are discussed next.

3.2. Kinetic Energy Ratio, H^2/V^2

[23] Considering far field earthquake records, the two end member propagation regimes ballistic and diffuse are associated with direct *P*- and *S*-wave arrivals, and multiply scattered coda waves, respectively. In the latter case, energy transport can be described with a diffusion process. Modal equipartition, implying no net energy flux, can not be reached in an open system like the Earth's crust, and constitutes therefore an asymptotic limit. Based on theoretical arguments, a marker for equipartition is the temporal stabilization of the *S*-to-*P* deformation energy ratio [*Weaver*, 1982; *Shapiro et al.*, 2000; *Hennino et al.*, 2001; *Margerin et al.*, 2009; *Sánchez-Sesma et al.*, 2011]. Recall that equipartition implies equilibration, yet the converse statement does not hold since equilibration can occur before equipartition is reached [*Paul et al.*, 2005]. Equilibration refers to the concept that mode conversion through scattering is balanced, and hence energy ratio markers are stable. The ratio depends on the scattering and absorption properties. A stabilized energy ratio is a good indicator "that the field is entering a regime in which total energy is described by a diffusion and will therefore evolve towards equipartition and isotropy" [*Campillo*, 2006]. However, the diffusion approximation largely underestimates flux anisotropy [*Paul et al.*, 2005]. Moreover, considering the ambient seismic field in an open medium, energy ratio stabilization can also result from close proximity to a constant source process.

[24] We note that estimates of deformation energy require specific network geometries to compute spatial derivatives of the wave field [*Shapiro et al.*, 2000; *Margerin et al.*, 2009]. Strain and kinetic energy densities are equal when both are averaged over one or more wavelengths [*Margerin et al.*, 2009]. Hence, the stabilization of the kinetic energy ratio, H^2/V^2, can alternatively be used as a proxy to indicate a diffusive regime [*Hennino et al.*, 2001]. Since properties of earthquake coda waves are insensitive to the source process and are thus associated with randomization effects of the medium, we study the noise-H^2/V^2 level and compare it to corresponding coda results. That is, we compare H^2/V^2 of pre-*P*-phase noise to coda-H^2/V^2 of 35 local and regional $M_l > 5$ earthquakes (Figure 1a). Details of the processing can be found in Appendix A.

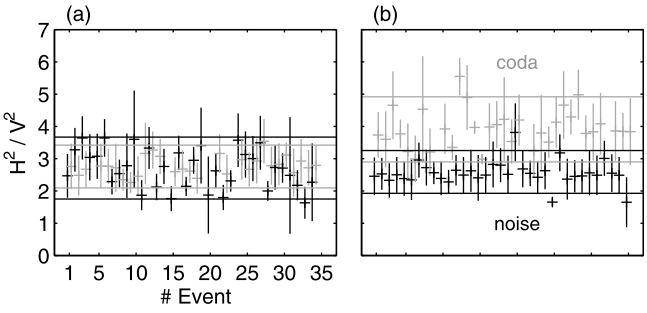

Figure 4. Comparison of kinetic energy ratio distributions, H^2/V^2, for noise (black) and earthquake coda (grey), in the 2–4 Hz range. Coda signals from 35 earthquakes (depth 8–172 km; M_l5–6.9; horizontal distance 46–359 km; Figure 1) are used. Crosses and error bars indicate mean and time-dependent fluctuations for coda and noise analysis windows associated with each earthquake. Black and grey horizontal lines show the standard deviation of the corresponding total population. Results from (a) the TDCB surface station and (b) the borehole sensor BHS4. Key observations are similar noise and coda levels at the surface, and different levels at depth. All values exceed the theoretical estimates of H^2/V^2 at $z = 0$, 1.8, and $z = \infty$, 2 [*Hennino et al.*, 2001].

[25] Despite the random sampling of the noise windows, estimates of noise-H^2/V^2 are remarkably stable for most sensors and frequencies (Figure 4), and the amplitudes of temporal fluctuations are similar for coda and noise. The levels of noise- and coda-H^2/V^2 ratios are more similar at the surface station (Figure 4a) compared to borehole observations. At depth (Figure 4b), coda-ratios are consistently larger compared to noise-ratios. While noise-ratios are relatively stable across the array, coda-ratios tend to further increase with depth.

[26] We find that coda-ratios are relatively insensitive to frequency while noise-ratios show a weak frequency dependence for the lower three bands. For the high-frequency band (8–16 Hz) significantly different and fluctuating noise-ratios indicate that the noise wave field is no longer controlled by a stable source mechanism and/or propagation regime. The analyzed signals may thus not be associated with actual ground motion. This is compatible with the overall decay of noise amplitudes and the associated sensitivity to electronic noise above ~6 Hz (Figure 2b). Larger amplitude coda waves do not suffer from these artifacts.

[27] Theoretical estimates of H^2/V^2 in a homogeneous half space at $z = 0$ and $z = \infty$ are 1.8 and 2 [*Hennino et al.*, 2001], respectively, and thus underestimate our measurements. Consistent with the depth dependent noise amplitude distribution (section 3.1), larger discrepancies at deeper sensors located in the Chinshui Shale suggest a more effective trapping of transversal wave energy in the layer. Systematic deviations from half space partition-ratio estimates can be explained by the stratified propagation medium [*Margerin et al.*, 2009; *Sánchez-Sesma et al.*, 2011; *Nakahara and Margerin*, 2011]. The dipping layer structure implies significant variations in the constituents of the wave field and therefore of ratio fluctuations over sub-wavelength depth intervals. Velocity information (Figure 1b) are valuable resources to estimate the equipartition-ratio numerically. However, missing information about the lateral velocity structure of the complicated dipping tectonics, which is characterized by the dipping Chinshui Shale and Kueichulin Formation sandwiched between the Cholan Formation [e.g., *Wu et al.*, 2007, Figure 1b], hampers reliable estimates.

[28] Systematic differences between noise- and coda-ratios indicate variable constituents of the two wave fields. The observed coda-ratio stabilization can readily be attributed to equipartition [*Campillo and Paul*, 2003]. In contrast, noise-ratio stabilization can be associated with a source process that is sufficiently stable in time. The observed larger coda-ratios highlight the relatively low transversal energy in the noise wave field. This is consistent with the general observation that anthropogenic noise is dominated by *P*- and Rayleigh waves. Nevertheless, noise-ratios >2 are consistent with the amplitude pattern observed in section 3.1, i.e., vertical component amplitudes are smaller compared to horizontal amplitudes. We conclude that emitted *P*-wave energy is scattered to *S*-wave energy, but that this process is not equilibrated. In other words, the constant flux of longitudinally polarized waves prevents to observe the equipartition in scattered waves.

[29] It is intriguing that the best agreement between predicted and observed ratios is found at the TDCB surface sensor, in contrast to the results of *Nakahara and Margerin* [2011]. It implies a significant effect of the material in the upper 1000 m on both wave fields, which is also indicated by the different coda-ratio levels. Scattering at topographic irregularities [*Ma et al.*, 2007] and the greater distance of TDCB to the source area (Figure 1a) facilitate randomization. The wave field is no longer dominated by the ballistic components as at TCDP.

[30] An independent assessment of the scattering or transport mean free path informs the estimate of the dominating propagation regime. The randomness of media is usually parametrized by the fluctuation power spectrum, or, equivalently, by the fluctuation autocorrelation. Inappropriate as it may be, we assume a $e^{-r/a}$ parametrization to evaluate the order of magnitude of the fluctuation length scale [*Aki and Richards*, 1980; *Frankel and Clayton*, 1986]. Here, r denotes the distance lag of the $v_P(z)$ (Figure 1b) autocorrelation and a is the "correlation distance of inhomogeneity." Generally, estimates of the fractional loss of energy for a wave with wave number k require information about the scale of the heterogeneous body or travel distance L. However, a discussion of the present situation in terms of a *ka*-*kL* diagram [*Aki and Richards*, 1980, section 13.3.5] is perhaps more illuminating than a determination of energy loss. We find that $e^{-r/a}$ functions with $a \approx 20$ m best fit the v_P autocorrelation function. Hence, for a 4 Hz wave traveling at 4 km/s, $k = 6 \times 10^{-3}\mathrm{m}^{-1}$ and ka is of order 10^{-1}. Without an estimate of L, we can readily see that the sampled medium can be characterized by an 'equivalent homogeneous body' (referring to results in section 4.1, L is of order 10–50 km, considering the distance between the TCDP site and the coast for the inferred azimuth distribution). In other words, the fluctuations are too small-scale with respect to the wavelengths considered here, leading to unrealistic large scattering mean free paths after a determination of scattering Q. This conclusion is, however, preliminary since it depends on the limited depth interval of the sample. Moreover, the above approximation is based on an isotropic fluctuation distribution. Useful as the in-situ observations

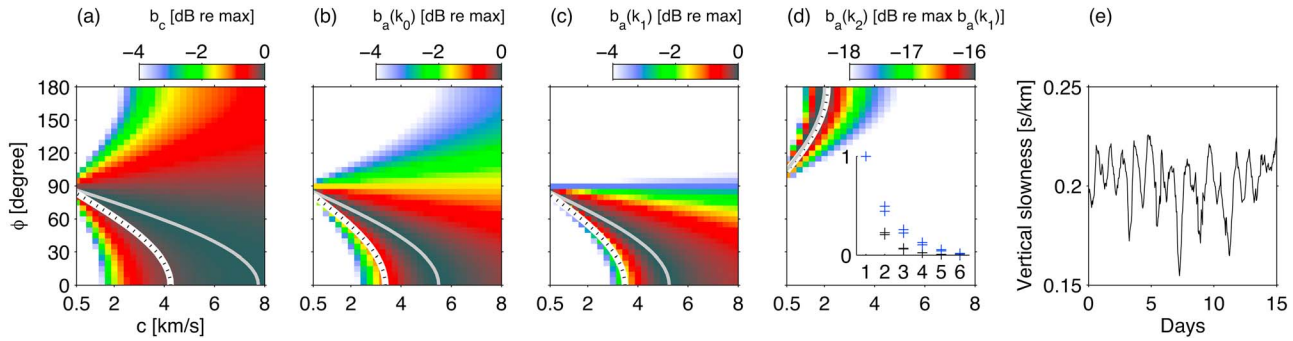

Figure 5. Typical vertical-component beamformer output using data from GMT day-time hour 7, from February 3, 2009, in the frequency band 2.75–3.25 Hz (Figures 5a–5d). (a) Conventional estimate, b_c. Adaptive estimate, b_a, inverted using (b) no decomposition of the cross spectral density matrix **C**, the (c) largest and (d) second largest eigenvalue of the decomposed matrix $\widetilde{\mathbf{C}}$ (Appendix B). Decibel reference values are the respective maximum values, except for Figure 5d, which is scaled by the maximum value of Figure 5c to highlight the significant difference between up- and downward propagating energy. In Figures 5a–5d grey and black dotted lines indicate vertical slowness estimates from beamforming applied to the Z- and N-, E-components, respectively. The inset in Figure 5d shows the averaged, scaled eigenvalues k_n, $n = 1, \ldots, 6$ associated with seven days of Z-component data in February 2009. Black and blue symbols correspond to the two lower and higher frequency bands, respectively. (e) Diurnal fluctuations of slowness estimates from $b_a(k_0)$, hourly sampled and smoothed with a 6-h moving average. Vertical-component data, 2.75–3.25 Hz.

are in multiple other contexts, 2-dimensional velocity distributions over a larger scale yet at lower resolution are required to estimate the scattering properties in the considered frequency range more accurately.

[31] In conclusion, the stability of the coda-H^2/V^2 marker suggests that coda energy propagates in a regime that can be described by a diffusion process. Stabilization of the noise-ratio does not permit a corresponding conclusion. The temporally stable source process (Figure 2a) can lead to a similarly stable noise-H^2/V^2, which can still be dominated by ballistic propagation. Data on medium heterogeneity can not be utilized to assess relevant scattering properties. Additional tests targeting the randomization of wave propagation directions or flux isotropy—allowing an independent assessment of the multiple scattering regime [*Hennino et al.*, 2001]—are therefore examined in following sections.

3.3. Beamforming

[32] In the next two sections we estimate flux directions of coherent energy. It facilitates the assessment of wave field randomization and noise source distribution. Estimates of the degree of isotropy also explain differences between noise correlation functions and impulse responses. First, we apply plane wave beamforming to each of the three components of the six-sensor array. We reduce the original bandwidths Δf by a factor 4 to obtain narrow band signals that facilitate the beamforming approach. Two estimates are computed: The 'conventional' b_c and 'adaptive' b_a beamformer output (Figures 5a–5d). Details of the processing can be found in Appendix B.

[33] The vertical geometry of the array does not allow an azimuthal resolution of the arriving coherent energy. We measure the compatibility of the data with a plane wave model that is phase shifted through a range of incidence angles ϕ and phase velocities c, synonymous with estimates of the vertical slowness $s = \cos(\phi)/c$. Except for the high-frequency band, conventional beamformer outputs consistently indicate incidence angles smaller than 90° (Figure 5 and Table 1). This implies that coherent wave field energy can be parametrized by plane waves that cross the array in a predominantly upward direction. Slowness estimates derived from horizontal-component beamforming are systematically larger compared to estimates associated with the Z-component. But a shear propagation speed $c = v_S = 2$ km/s results in incidence angle estimates that are consistent with the vertical-component results (Table 1).

[34] Adaptive beamforming can be utilized in two ways. First, the output b_a associated with no decomposition of the cross spectral density matrix **C** (Appendix B) is characterized by an increased resolution compared to b_c (Figures 5b and 5c). The result suggest—consistent with the conventional results—that the dominant part of coherent energy is arriving from below. Second, a singular value decomposition of **C** allows the separation of multiple sources. The b_a output that corresponds to a $\widetilde{\mathbf{C}}$-matrix, which is associated with a singular value k_n, $n = 1, \ldots, N$, indicates a separate direction of coherent energy flux. The number of singular values N equals the number of array sensors. In practice, the method succeeds when the first one or two eigenvalues are significantly different from zero. A slower decay of eigenvalues signals problems in the decomposition of the data into separate orthonormal bases. The scaled eigenvalues k_n for the four narrow bands averaged over 15 days for the Z-component analysis are plotted in the inset in Figure 5d. Results for the N- and E-component analysis are similar.

[35] It shows that the dominant part of the energy—corresponding to the largest eigenvalue k_1—is consistently associated with upward traveling waves (Figure 5c). Note that decomposition has further increased the resolution. For the two lower frequency bands, the second eigenvalue k_2 is roughly an order of magnitude smaller. Compared to the k_1 solution the output of the associated $b_a(k_2)$ estimate is much smaller (Figure 5d). This is synonymous with a significantly decreased compatibility of the wave field with the plane

wave parametrization. It indicates decreased amplitudes of the coherent waves compared to uncorrelated fluctuations. We find that slowness estimates as in the example shown in Figure 5d are less stable compared to values associated with k_1 (Figure 5c). Together, these results suggest the resolution of coherent wave energy with a predominantly downward propagation direction. The stability of the solution, and the plane wave approximation are however significantly reduced compared to the $b_a(k_1)$ solution associated with upward energy flux.

[36] The frequency dependence of the k_n (inset in Figure 5d) suggests that the decomposition of the wave field into separate ballistic components is less successful at higher frequencies. That is, the increased similarity between k_1 and k_2 indicates an increased difficulty to parametrize and interpret a more complex wave propagation situation using a simple model; and hence a better randomization of propagation directions. This conclusion is supported by a similar frequency-dependent decreasing consistency of the wave field to an incident plane wave model. That is, peak beamformer outputs decrease with increasing frequency (not shown), indicating that propagation directions become increasingly isotropic. The two measurements are as well compatible with frequency-dependent randomization properties of the medium, as with a spatially better averaged high-frequency source distribution.

[37] Hourly slowness estimates derived from the adaptive beamformer output $b_a(k_0)$ (no decomposition; Appendix B) are dominated by diurnal fluctuations (Figure 5e). This pattern is associated with the anthropogenic source process, similar to noise amplitude behavior (section 3.1, Figure 2a). The slowness for all three components of the low-frequency band peaks during the day, while the slowness time series $s(t)$ for the three higher frequencies shows a ~12-hour phase shift. Amplitudes of the diurnal changes vary with frequency (not shown). That is, $s(t)$ amplitudes for high frequencies are larger compared to the behavior at low frequencies, and thus carry the footprint of source fluctuations.

[38] The cultural origin of the noise wave field, which is assumed to be generated at the surface, and the predominant upward propagation of coherent wave energy seem paradox. To estimate the azimuthal direction to better localize the noise source regions, we apply a polarization analysis to the direct arrival of noise correlation functions (section 4.1). With prejudice to the results of this analysis, we take the view that wave energy is excited at the surface of the Earth—in the lowlands of western Taiwan—and then follows a trajectory similar to ballistic waves traveling in a medium with a positive velocity-depth gradient.

[39] To conclude, the analysis of the ambient wave field revealed an anthropogenic source process, stabilized kinetic energy ratios, and an anisotropic, upward propagation of coherent energy. These results imply that the propagation regime is dominated by a ballistic component. A scattered wave field component coexists; it appears weaker but is not negligible, and it becomes increasingly important at higher frequencies. The wave field evolution towards a more diffuse regime is prevented by the constant supply of energy associated with a stable excitation process—at least for the time period considered. Consequences for the construction of noise correlation functions and the resulting implications for potential monitoring efforts are investigated in the next section.

4. Cross Correlation of Ambient Noise

[40] We briefly discuss basic theoretical properties associated with noise correlation functions, hereafter termed C^1 functions, that are relevant for our analysis. In the case of homogeneous inelastic absorption properties, the correlation function of isotropic, scattered wave fields recorded at two sensors located at x_A, x_B is proportional to the Green's function $G(x_A, x_B, \tau)$ including all reflected and scattered modes, i.e., $\partial_\tau C^1(x_A, x_B, \tau) \propto G^+(x_A, x_B, \tau) - G^-(x_A, x_B, \tau)$ [e.g., *Lobkis and Weaver*, 2001]. Here, τ is the correlation time lag, G^+ and G^- denote the causal and anti-causal Green's function, respectively, and $\partial_\tau C^1$ abbreviates $\partial C^1/\partial\tau$. Reconstruction of G is guaranteed only if the wave field is near isotropic, i.e., if it approaches equipartition [*Weaver*, 1982]. The obtained C^1 functions can be analyzed with standard imaging and monitoring techniques [*Shapiro et al.*, 2005; *Sens-Schönfelder and Wegler*, 2006; *Brenguier et al.*, 2008]. Even if the wave field is not perfectly equipartitioned yet characterized by a stable *S*-to-*P* energy partition, converged C^1 functions can be used for monitoring purposes [*Hadziioannou et al.*, 2009]. Details of the processing regarding the construction of the 15 individual C^1 functions between the six TCDP sensors are described in Appendix C.

4.1. Polarization Analysis

[41] We continue with the implementation of additional tests addressed in section 3.2 to estimate wave propagation directions and hence the randomization of the wave field. To compensate for the lack of azimuthal resolution associated with the beamforming analysis (section 3.3), we apply a polarization and particle motion analysis to the main arrival of C^1 functions (Appendix D). *Landès et al.* [2010] demonstrated that—for plane *P*-waves—the covariance matrix **C** of a single 3-component record differs only by a scalar from the matrix **C** constructed from the ZN-, ZE-, and ZZ-C^1 functions associated with a sensor pair. Following this approach, we compute the three C^1 functions for each sensor pair, and estimate incidence angle ϕ, azimuth θ, and rectilinearity R from the 15 correlation matrices. Note that the determination of the azimuth θ tunes the analysis to *P*-wave motion. We tested the method comparing 3-correlation results to 3-component results from an analysis of *P*-wave arrivals from the 35 regional earthquakes used in section 3.2. Considering the complex structure across the array, we find a good agreement between the two approaches which supports the applicability of the 3-correlation polarization analysis. Estimates of incidence angle, azimuth, and rectilinearity are generally insensitive to daytime and frequency, except for results associated with the high-frequency band 8–16 Hz, which are separately discussed.

4.1.1. Incidence Angle

[42] For *P*-wave motion, the measured incidence angles (Figures 6a and 6b) for the two center frequency bands, 27° and 24°, agree with estimates from vertical-component beamforming, 37° and 41°, using slowness estimates and in-situ wave speeds (Table 1). It confirms the predominant upward propagation of coherent noise energy. Mean incidence angles

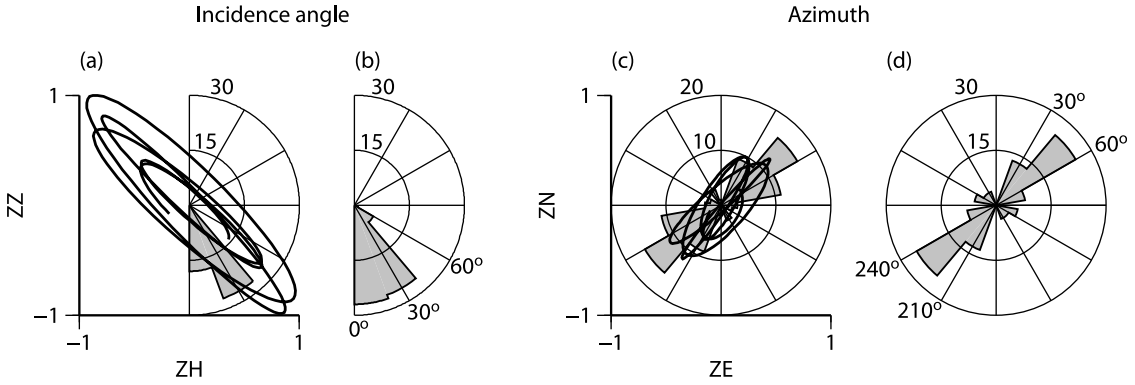

Figure 6. Estimates of incidence angle (rose diagram in Figures 6a and 6b), azimuth (rose diagram in Figures 6c and 6d), and typical particle motions (black lines in Figures 6a and 6c) obtained from the correlation-based polarization analysis. Particle motions are plotted for pair BHS1-BHS4, 1–2 Hz, 24-h data, and scaled to the maximum ZZ-C^1 amplitude. The bin width in the rose diagrams is 20°. Statistics are taken from the 15 inter-sensor results. (a) Incidence angle. Cumulative time of day dependence for the 1–2 Hz band. Results from day- and night-time and 24-h C^1 functions are stacked. (b) Incidence angle. Results from 24-h C^1 functions from the four frequency bands are stacked. (c) Azimuth. Cumulative time of day dependence. (d) Azimuth. Stacking as in Figure 6b. Data around $\theta = 120°$ that deviate from the main 45° trend correspond to high frequencies.

for the low- and high-frequency band (25°, 26°) are very similar to angles associated with the two intermediate bands, but are significantly smaller compared to values obtained from the Z-, N-, and E-component beamforming analysis (>70°). We attribute the consistently lower ϕ estimates from the C^1-based polarization analysis to an increased sensitivity of the C^1 functions to waves traveling along the receiver alignment. That is, only sources—or scattering events—along the receiver-connecting path interfere constructively. This end-fire lobe sensitivity is discussed in section 4.3 in more detail.

4.1.2. Azimuth

[43] Azimuth estimates show a stable 30° to 50° pattern (Figure 6c). While earthquake *P*-wave motion can be used to resolve the azimuthal 180° ambiguity, this is not possible using noise correlations. However, the geographical distribution of inferred noise sources relative to the recording location favors directions to the South-West over North-East bearings. This is because directions at $\theta \approx 40°$ point towards the mountain range dominating the central part of Taiwan. Opposite bearings at $\theta \approx 220°$ point towards the lowlands at the foot of the mountain range in which the borehole experiment is located (Figure 1). We thus consider that high-frequency cultural noise is excited in these densely populated areas. Note, however, that the dominating source process is not necessarily located along a 220° bearing; i.e., local particle motion can differ from the actual propagation direction (Appendix D).

[44] Incidence angle and azimuth estimates in the 8–16 Hz band—and to a lesser degree in the 4–8 Hz band—show higher fluctuations between the 15 individual measurements compared to lower frequencies. This is consistent with the frequency dependent eigenvalue pattern and beamformer output (section 3.3). Whereas beamforming results could not definitely discriminate between source and medium effects, higher fluctuations between the C^1-based estimates are associated with scattering in the medium. A dominant source effect could not lead to increasingly irregular direction estimates at sub-wavelength scales across the array (16 Hz *P*-wave length: 250 m; sensor spacing: 50 m). We conclude an increased sensitivity of shorter wavelengths to the complex environment.

4.1.3. Rectilinearity

[45] Estimates of rectilinearity are, except for values around 0.9 for the 8–16 Hz range, practically equal to unity. Figures 6a and 6c show typical particle motions associated with the ZN-, ZE-, and ZZ-C^1 functions for station pair BHS1-BHS4. Recalling the definition for this measure, $R = 1 - (\lambda_1 + \lambda_2)/2/\lambda_0$, with $\lambda_{[0,1,2]}$ denoting the ordered eigenvalues of the covariance matrix, we remind that $R \approx 1$ indicates motion that is "confined predominantely to a subspace spanned by a single eigenvector, […] a characteristic of *P*, *SH*, and precritical *SV* body waves and Love surface waves" [*Wagner and Owens*, 1996]. Since the analysis it tuned to *P*-waves, we conclude that the C^1 direct arrivals correspond to longitudinal body waves. A focus on transversal energy propagation requires the adaptation of the analysis technique to *S*-wave propagation. Possible contributions of head waves trapped in low-velocity layers within the Chinshui layer can not be excluded.

[46] As an interim result, the C^1-based polarization analysis supports the upward propagation direction of coherent noise energy. Reminding us of the unresolved estimate of the diffuse component, the frequency dependent broadening of the azimuthal distribution can be associated with an increasing wave field randomization due to scattering. The conjecture of a more homogeneous spatial distribution of high-frequency sources is less compatible with this observation. It leads to a similar decrease in observed anisotropy, but it does not imply more multiply-scattered waves. Further evidence targeted at this ambiguity comes from the study of C^1 functions. In the next sections we focus on properties of C^1 functions, which depend on previously discussed noise properties and allow independent conclusions about the character of the wave field from which they are constructed.

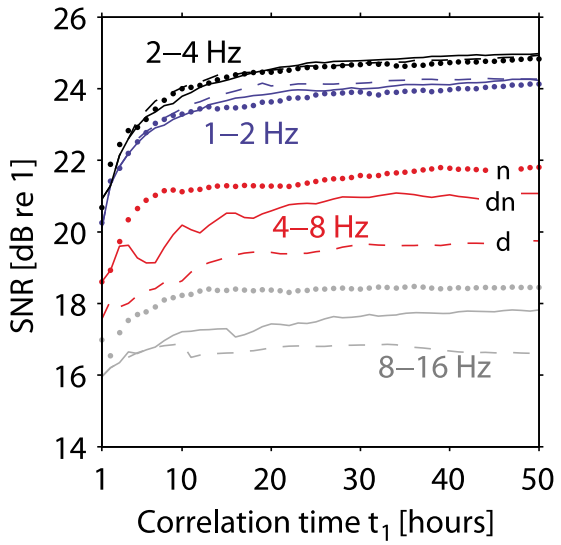

Figure 7. Evolution of the C^1 signal-to-noise ratio (SNR) as a function of correlation time, t_1. The functions are the mean SNR from the 15 inter-sensor ZZ correlation pairs. Lower-case d, n, dn denote C^1 functions constructed using only day- or night-time data, or 24-h data, respectively.

4.2. C^1 Convergence

[47] A marker for the coherence build-up in a correlation function is the evolution of the C^1 signal-to-noise ratio (SNR) as a function of correlation time or record duration, t_1. Here, 'signal' is the maximum amplitude of the direct arrival measured in the lag window between −0.5 and 0.5 s, and 'noise' is the amplitude standard deviation in the C^1 coda. It is measured in windows between 20 and 50 times the frequency band central period $T_c = 1/f_c$ [*Sabra et al.*, 2005a]. We study the convergence rate of ZZ-C^1 functions in the four frequency bands using the original bandwidths $\Delta f = 1, 2, 4, 8$ Hz. Convergence describes the negligibility of residual fluctuations compared to a reference impulse response [*Larose et al.*, 2007], or, more generally, the asymptotic behavior of a SNR(t_1) function. It is well established that the SNR of correlation functions evolves proportional to the square root of the length of the correlated time series, t_1 [*Weaver and Lobkis*, 2005; *Sabra et al.*, 2005b]

$$\mathrm{SNR} \propto \sqrt{t_1}. \tag{1}$$

Figure 7 illustrates this behavior of the average SNR(t_1) functions. The SNR level increases in response to the stacking process, by which coherent energy builds up in the main arrival while simultaneously remnant fluctuations in the coda decrease. More specifically, the SNR evolution follows [*Larose et al.*, 2007]

$$\mathrm{SNR} \propto B\sqrt{\frac{t_1 c \Delta f}{d^e f_c}}, \tag{2}$$

where B is a parameter that describes noise intensity [*Weaver and Lobkis*, 2005; *Weaver et al.*, 2009; *Weaver*, 2011], and c, Δf, d, e, and f_c denote phase velocity, bandwidth, sensor distance, a fit exponent, and central frequency. In our case, the predicted SNR increase with Δf is counterbalanced by the simultaneous increase of f_c. The constant $\Delta f/f_c$ ratio suggests, together with frequency independent t_1, c, d, and e, that an inverse frequency dependent noise intensity B controls the lower SNR levels at higher frequencies. The lower 1–2 Hz level compared to the 2–4 Hz level can be explained by the reduced sensitivity of the recording equipment (Figure 2). *Wang et al.* [2012] show that Q is frequency independent between 2 and 40 Hz below ∼1 km depth in the recording environment. We conclude that smaller high-frequency noise intensities are associated with anthropogenic activity, which includes weaker sources at and stronger absorption near the surface, respectively. This is consistent with the decreasing amplitude level for $f > 5$ Hz (Figure 2b).

[48] While day- and night-time and 24-h SNR functions at lower frequencies show little variability, high-frequency C^1 functions constructed from data recorded during night-time hours display a significantly higher coherence level compared to day-time C^1 functions (Figure 7). Recall that the diurnal amplitude pattern (Figure 2a) shows low night-time amplitudes across the considered frequency range. It indicates that noise amplitudes do not necessarily correlate with the coherence level of the associated wave field.

[49] The analysis shows that the SNR levels saturate after correlating about 10 and 20 hours of high- and low-frequency data, respectively. Considering the high SNR levels at f_c = 1.5 and 3 Hz, a 24-h correlation is better converged compared to a 9-h day-time correlation. We conclude that it is favorable to utilize daily C^1 functions in the lower frequency range in future monitoring efforts.

4.3. C^1 Direct Arrival

[50] The C^1 arrival time allows the estimate of seismic velocities between two sensors. The arrival pulse width Δt is inverse proportional to Δf; e.g., for the 1–2 Hz band, Δt = 0.5 s. In the case of an isotropic noise wave field, we expect for $-0.25\ \mathrm{s} < \tau < 0.25$ s the associated symmetric arrivals to interfere. This interference leads to a pulse symmetric to $\tau = 0$, which does thus not allow a velocity estimate. Instead, the direct arrival of the C^1 function shows a pronounced one-sided pulse at negative correlation lags (Figure 8a). The C^1 asymmetry results from the anisotropic propagation of noise energy [*Larose et al.*, 2005; *Paul et al.*, 2005; *Stehly et al.*, 2006]. The concentration of energy at negative lags is associated with energy propagating from deeper to shallower sensors, consistent with the beamformer slowness estimates and incidence angle estimates from the polarization analysis. The distance dependent decrease of the amplitude (Figure 8b) is associated with attenuation and geometrical spreading [*Larose et al.*, 2007; *Gouédard et al.*, 2008; *Cupillard et al.*, 2011; *Prieto et al.*, 2011].

[51] We measure phase velocities across the array using ZZ-, EE-, and NN-$\partial_\tau C^1$ functions (Appendix E). In contrast to the averaging beamforming approach the variability pattern or results associated with different sensor pairs allows an increased spatial resolution of local wave field properties. Our measurements show that velocities on vertical channels are generally larger compared to horizontal estimates, consistent with logged P- and S-wave velocities. However, we find significant fluctuations between the measurements across the array. Similar to the SNR pattern higher velocities are obtained between closely spaced sensors that are predominantly located around the network center (Figure S1, panels a–c, in the

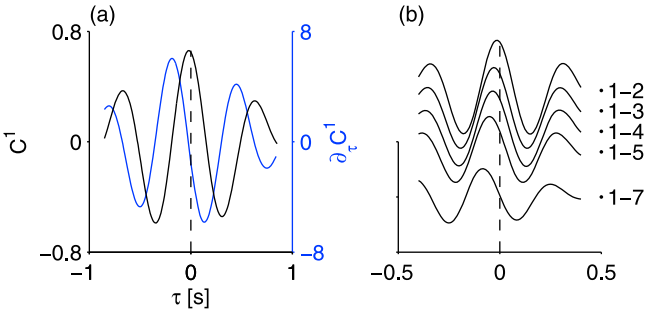

Figure 8. Direct arrivals of C^1 correlation functions. (a) C^1 (black) and $\partial_\tau C^1$ (blue) for correlation pair BHS1-BHS4, in the 1–2 Hz range. Both functions are analyzed to estimate the propagation speed of the main arrival across the network. (b) Inter-sensor C^1 functions at 2–4 Hz illustrate the propagating pulse. Reference sensor is the top sensor BHS1. The ordinate is on the same scale as in Figure 8a. Zero levels for individual correlation pairs, indicated by the black dots, are offset according to sensor distance.

auxiliary material).[1] Velocities measured between more distant, mostly peripheral sensors are usually lower and in better agreement with in-situ values. In addition to the *dz* dependent aperture effect discussed below, we consider the possibility that direct arrival waveforms of correlations from neighbored pairs are distorted. They are biased by small amplitudes at positive correlation lags associated with downward traveling energy. The existence of downward propagation was indicated by Figure 5d, and will be further substantiated in section 5.

[52] To select estimates for the assessment of an average phase velocity, we tested several criteria based on absolute and relative amplitude of the main arrival, and on sensor distance *dz*. We choose to average over values associated with sensor pairs in the three lower frequency bands that are separated more than 1/5 of the wavelength regardless of amplitude, i.e., $dz \geq \lambda/5$, where λ is the wavelength (in-situ $[v_P, v_S] \times T_c$). Keeping the resulting sample distribution of a certain size motivates the factor 1/5. The resulting median values are given in Table 1.

[53] Are we measuring apparent or true velocities? A propagation regime dominated by anisotropic ballistic waves results in arrivals associated with the apparent travel time [*Gouédard et al.*, 2008]. Diffuse wave fields consisting of an anisotropic component can still result in C^1 functions that contain a phase shift compared to the impulse response. However, the error is found to be small [*Weaver et al.*, 2009], especially for multiply scattered coda waves compared to ballistic arrivals. This can be explained by the stationary phase theorem [*Froment et al.*, 2010, and references therein]. It predicts that contributions to the reconstruction of the Green's function travel in the receiver alignment within an aperture that depends on $\sqrt{\lambda/dz}$.

[54] We infer that—using an incidence angle of 40°—the velocity estimates are not large enough to be compatible with apparent velocities exclusively associated with the ballistic component. The aperture dependent approach also explains why measurements between more distant sensors are in better agreement with the in-situ velocities (Figure S1, panels a–c), i.e., because of narrowed end-fire lobes. Lower frequencies increase the aperture, and velocities are thus larger, i.e., become more apparent (Table 1). Smaller incidence angles obtained from the C^1-based polarization analysis compared to beamforming estimates (Table 1) are also consistent with this concept.

[55] In conclusion, properties of C^1 direct arrivals are not exclusively controlled by the ballistic properties of the ambient wave field, as inferred from the beamforming analysis. The reconstruction of near in-situ phase velocities, especially for more distant sensors, indicates a relevant scattered component in the noise.

4.4. C^1 Coda

[56] Cross correlation separates the ballistic from the scattered or diffuse component in the noise. Since C^1 functions are approximations of impulse response, C^1 coda displayed in Figure 12 proves the existence of a scattering. We can therefore conclude that the ballistic and scattered propagation regime coexist in the TCDP noise.

[57] Noise-based monitoring exploits information about seismic velocity changes in the propagation medium that accumulate in the arrival time of C^1 coda phases [e.g., *Wegler and Sens-Schönfelder*, 2007; *Brenguier et al.*, 2008; *Meier et al.*, 2010; *Chen et al.*, 2010; *Rivet et al.*, 2011]. The analysis is performed on coda time windows that are short compared to the above SNR 'noise' window. The window usually begins at several multiples of the direct arrival time to exclude effects associated with the direct wave, and extends to lags that include coda phases which show a relatively good coherence over the observation period. Here, we evaluate properties of C^1 coda in a time window between 5 and 25 times T_c (Figure 9), using converged correlation functions constructed from 24-h data.

[58] A key observation of the coda analysis is the significantly higher symmetry compared to the asymmetric main arrival. This conclusion is unaffected by the exact choice of the analyzed time window. A proxy for the increased symmetry is the balanced energy ratio of coda segments of negative- and positive-lag windows across all correlation pairs and frequencies. The improved symmetry is a consequence of scattering in the propagation medium. Despite the more symmetric energy distribution in the C^1 coda, individual waveforms and the associated spectrograms are characterized by asymmetric arrivals and an associated variable frequency content at opposite sign lags (Figure 9; e.g., waveforms around $\tau/T_c = \pm 20$). It demonstrates that scattering does not completely eliminate effects associated with anisotropic noise excitation. It is compatible with the concept developed in section 3.2, i.e., the observational site is too close to the source area to allow a large number of scattering events. As a consequence, scattered wave paths are not sampled uniformly [*Hadziioannou et al.*, 2009].

[59] Techniques to estimate variations of coda phase arrival times such as the doublet [*Poupinet et al.*, 1984; *Brenguier et al.*, 2008] or stretching [*Wegler and Sens-Schönfelder*, 2007] method are usually applied to positive and negative lags simultaneously. This procedure is justified for symmetric C^1 functions obtained from an isotropic, diffuse wave field, since scattered wave paths are sampled uniformly in both directions. Asymmetric arrivals in the C^1

[1] Auxiliary materials are available in the HTML. doi:10.1029/2011JB008999.

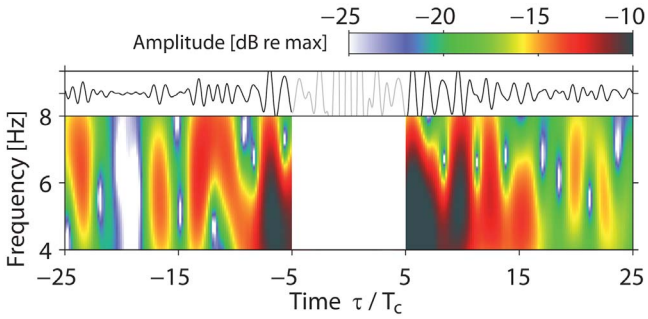

Figure 9. C^1 coda for the correlation pair BHS3-BHS5 at 4–8 Hz. The time series on top shows C^1 as a function of correlation lag time, τ, scaled by the frequency band central period, T_c. The C^1 amplitude range is [−0.04 0.04]. Spectral amplitudes are scaled to the maximum amplitude of the main arrival.

coda suggest that averaging over negative and positive lags possibly biases travel time change estimates. This effect may be amplified by the sensitivity to vertical propagation directions. That is, phases that correspond to a predominantly up- or downgoing wave field component are possibly sensitive to depth-dependent velocity changes.

[60] To summarize, a time-symmetric coda energy distribution implies a significant evolution towards isotropy of the C^1 coda wave field. This constitutes an observation of a multiply scattered wave field. The alternative explanation—a homogeneous source distribution down to 1–2 Hz—is incompatible with the observed narrow directivity estimates. Nevertheless, asymmetric coda arrival patterns are a footprint of the heterogeneous source distribution. Hence, properties of the original ambient noise wave field—such as propagation directivity—may still be present in the C^1 coda wave field, albeit much attenuated. In other words, C^1 coda waves are better—yet not fully—equipartitioned compared to the anisotropic ambient noise wave field from which they are constructed [*Stehly et al.*, 2008; *Froment et al.*, 2011].

5. Correlation of C^1 Coda

[61] The C^1 coda carries information about the scattering properties of the medium and is therefore analogous to earthquake coda [*Campillo and Paul*, 2003; *Paul et al.*, 2005]. This motivates the iteration of the correlation procedure, i.e., C^1 coda can be re-correlated to obtain the C^3 function—the correlation of the coda of the noise correlation. The correlation time needed for C^3 functions to converge is significantly reduced compared to C^1. The cause for this reduction is the extraction of coherent energy—by the correlation procedure—from the ambient noise wave field that is masked by incoherent fluctuations. Random fluctuations in the more isotropic C^1 coda are consequently reduced with respect to the ambient noise.

[62] To construct the C^3 function associated with a sensor pair at x_A, x_B of a N-sensor array, codas from C^1 functions associated with each sensor of the pair and the other $n = N - 2$ sensors in the array are correlated and stacked (see Appendix F for the construction of ZZ-C^3 functions.) Important for the analysis below, negative and positive parts are correlated separately, and subsequently stacked:

$$C^3(\tau') = \frac{1}{2}\left(C^{3-}(\tau') + C^{3+}(\tau')\right). \tag{3}$$

A consequence is that the remaining n stations serve as virtual sources, implying that the source density can be controlled to a certain extent [*Froment et al.*, 2011]. Hence, C^3 symmetry is associated with the sensor distribution around the path x_A-x_B and the scattering properties of the medium condensed in the C^1 coda.

5.1. C^3 Convergence

[63] We investigate the dependence of the C^3 SNR on the parameters t_1 and t_3. Recall that t_1 is the time window of the noise used to construct the C^1 functions (Figure 7), and t_3 is the C^1 coda window length, measured in multiples m of the central period, T_c. Similar to the correlation time dependence of the C^1 convergence, C^3 SNR is proportional to [*Froment et al.*, 2011]

$$\mathrm{SNR} \propto \sqrt{nt_3}. \tag{4}$$

That is, the quality of the C^3 function depends on the number of virtual sources. Using numerical experiments to quantify competing effects on the SNR evolution, *Larose et al.* [2008] demonstrated that the SNR also depends on the scattering properties of the medium.

[64] *Stehly et al.* [2008] and *Froment et al.* [2011] used t_3 = 1200 s, equal to m = 160 in the considered frequency band. This duration was found in a trial and error procedure to optimize the resulting C^3 function. In the context of noise-based monitoring, we are interested to determine a parameter set that results in a good SNR while simultaneously maintains a high temporal resolution. Tests using m = 100, 200, 300, and t_1 = 1, 2, 4, 8 hours indeed show that the theoretically suggested combination, m = 300, t_1 = 1 hour, yields the best C^3 SNR.

[65] We find that C^3 SNR levels are inverse proportional to frequency (Figure 10). This trend is associated with the original, inverse frequency dependent noise intensity. At the same time, the level of C^3 SNR is consistently smaller compared to C^1 results. The relatively few number of virtual sources, n = 4, together with $t_3 \ll t_1$ (equations (1) and (4)), prevents C^3 SNRs to reach associated C^1 levels [*Froment et al.*, 2011]. As a caveat, the nevertheless high C^3 SNR levels (at 1–2 Hz, C^1 SNR: 24 dB, C^3 SNR: 22.5 dB) emphasize the significantly reduced remnant fluctuations and the consequently increased isotropy of the C^1 coda wave field compared to ambient noise.

[66] In section 4 we concluded that t_1 = 24 h correlations are sufficient to produce stable C^1 functions in terms of the SNR evolution. Figure 10 indicates that good C^3 SNR levels associated with the lower frequency bands require at least 60 hours of ambient noise data, resulting in a minimum 2.5-fold decrease of the temporal resolution. The ticks at each SNR curve in Figure 10 indicate intervals of 1-hour C^1 coda correlations. That is, for the 1–2 Hz range, 60 hours of noise yield—with t_1 = 1 h, m = 300—3 hours of C^1 coda correlations. It demonstrates the efficiency of the correlation

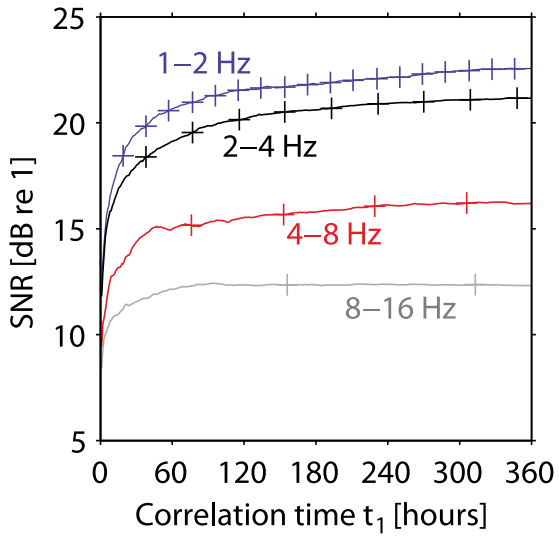

Figure 10. Evolution of the mean C^3 SNR(t_1) functions. Ticks mark intervals of one hour of correlated C^1 coda. The abscissa is identical to Figure 7 to facilitate the comparison of the temporal resolution.

procedure to separate coherent information from remnant fluctuations in the noise.

[67] Focusing on the SNR level of individual pairs, we find that peak values are systematically found for sensor pairs located predominantly in the center of the array, followed by lower levels associated with top or bottom peripheral pairs, and the lowest coherence is measured for sensors at opposite ends (see grey-scale pattern in Figure S1, panels d and e). This observation can be explained by the virtual source effect of the remaining sensors: Central pairs are equally surrounded by sources, end-member pairs have at least most sources located at one side, while opposite-side pairs have sources in between.

5.2. C^3 Direct Arrival

[68] The averaged C^3 function (equation (3)) used in the previous convergence analysis meets the expectation of two interfering, symmetric C^{3-} and C^{3+} pulses, i.e., it is symmetric to $\tau' = 0$ (Figure 11a). The two functions interfere destructively at the correlation pair BHS1-BHS5. Note that C^3 coda fluctuations also destructively interfere, such that the SNR estimates are not systematically biased by this effect. No propagating pulse emerges as in the C^1 case, confirming the isotropic energy distribution in the underlying C^1 coda wave field from which the C^3 functions are constructed. In contrast, individual C^{3-} and C^{3+} functions show an up- (Figure 11b) and downward (Figure 11c) propagating pulse. We observe a more rapid decrease of the coherence level with distance from the top sensor BHS1 compared to the C^1 result (Figure 8b). We attribute this to the virtual source effect, i.e., the source distribution changes for each correlation pair. In particular, sources are predominantly located either on one side of the pair (1–2, 1–3), or in between (1–5, 1–7), with the above discussed consequences.

[69] We repeat the phase velocity estimates from section 4.3 using C^{3-} and C^{3+} arrivals. Considering the pattern of individual C^{3-} and C^{3+} phase velocity measurements, we find that apparent wave propagation speeds between closely spaced sensors are generally increased, yet decreased between more distant sensors compared to the C^1 results (compare Figure S1, panels d and e, to Figure S1, panel a). This is visualized by the 'curved' moveouts in Figures 11b and 11c. We take the view that a combination of two effects is responsible for this distance dependent variability. First, some form of the oblique ambient noise wave field directionality is preserved in the C^1 coda. Second, anisotropic components of the noise wave field are possibly amplified by the anisotropic distribution of the virtual sources which includes sources between sensors. That is, averaging over the virtual sources is apparently not sufficient in the present context of a small 1-dimensional array. To what extend these results are generic, or a consequence of sensor geometry or present wave field or medium properties, has to be clarified by future numerical experiments or analyses of data recorded at different locations.

[70] The expected convergence towards in-situ wave speeds is met by averaging over values associated with sensor pairs with $dz \geq \lambda/5$ (Table 1d). The obtained $c = 4.1$ km/s —averaged over the 4–8 Hz C^{3-} and C^{3+} results—improves the corresponding C^1 estimate (Table 1c) and is compatible with the in-situ average $v_P = 4.0 \pm 0.3$ km/s. However, the still large variability between individual measurements in conjunction with the overall low SNR ratios, and the unsettled effect of the variable virtual source distributions leave a doubt concerning the conclusiveness of this estimate.

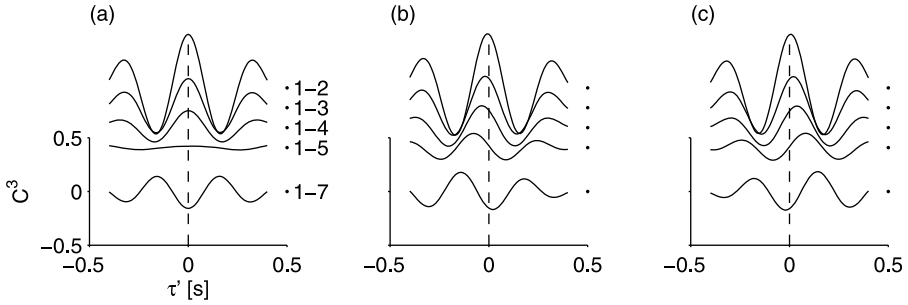

Figure 11. Direct arrivals of the (a) C^3, (b) C^{3-} and (c) C^{3+} functions at 2–4 Hz. We use the same conventions as in Figure 8b. We observe symmetric C^3 functions, whereas the C^{3-} and C^{3+} functions show an up- and downward propagating pulse, respectively. The moveout pattern is discussed in section 5.2 and quantified in Figure S1, panels d and e.

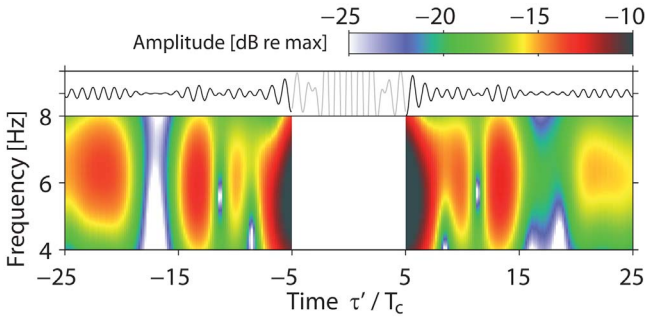

Figure 12. C^3 coda properties for the correlation pair BHS3-BHS5 at 4–8 Hz. We use the same conventions as in Figure 9. Note the overall higher symmetry compared to the C^1 coda result.

5.3. C^3 Coda

[71] Waveforms and spectral content of C^3 coda (Figure 12) exhibit an improved symmetry compared to C^1 coda (Figure 9). Consequently, energy partition between negative and positive C^3 coda windows is balanced on average as in the C^1 case. Negative windows from C^{3-} and C^{3+} contain more and less energy, respectively, compared to the corresponding positive coda windows. Improved coda symmetry indicates that C^3 coda waves further approached the equipartition limit. The asymptotic nature of this concept is visualized by the still not perfect, i.e., slightly asymmetric, arrivals (e.g., energy at lags $\tau'/T_c \approx \pm 18$, Figure 12). Supporting our conclusions from the C^1 coda analysis, it implies that some form of directivity from the original process remains in the C^1 coda wave field from which the C^3 functions are constructed.

[72] For monitoring applications, the increased symmetry of C^3 coda facilitates averaging over negative and positive lags. Together with the improved approximation to a diffuse, isotropic wave field, C^3 coda constitutes a useful complementary resource in monitoring efforts. The decreased temporal resolution with respect to the C^1 functions is balanced by the anticipated improved stability of the C^3 functions. This stability is associated with the reduced sensitivity to fluctuations in the background noise field that potentially bias the C^1 coda analysis. Using C^3 offers an alternative approach compared to previously tested C^1 denoising techniques [*Baig et al.*, 2009; *Stehly et al.*, 2011].

6. Discussion and Conclusions

[73] We analyzed systematically the ambient seismic wave field recorded by the TCDP downhole array around 1100 m depth in the frequency range between 1 and 16 Hz. Key observations obtained with various array processing and noise correlation techniques include a diurnal noise amplitude pattern and lowest amplitudes at the shallowest sensor; stabilized earthquake coda and noise kinetic energy ratios, with similar levels at a control surface stations, but relatively lower noise ratios in the borehole; predominantly upward propagating coherent energy, arriving from a narrow azimuthal range; a frequency dependent SNR level in noise correlation functions; strongly asymmetric C^1 direct arrivals, but significantly higher symmetry in C^1 coda properties; a similar frequency dependent SNR level in C^3 functions, which are characterized by a symmetric main arrival shape and even higher coda symmetry compared to the C^1 results.

[74] We find that results obtained with different techniques are generally consistent. Differences regarding individual measurements are associated with variable processing choices and variable—sometimes frequency dependent—sensitivities of the analyzed (meta) data to different properties or constituents of the ambient wave field. Complementary observations allow conclusions about the noise source process, estimates on the randomization properties of the propagation medium, and an assessment of the resulting wave field properties including its propagation regime.

[75] TCDP downhole high-frequency seismic noise is excited by an anthropogenic source process. The source distribution is confined to a narrow azimuthal range to the southwest of the recording site, coincident with the densely populated lowlands in western Taiwan. The observed ambient wave field is therefore controlled by a narrow spatial source distribution, resulting in a predominant anisotropic wave field component.

[76] Before we turn to a concluding discussion of the noise propagation regime, we recapitulate the relevant facts from the individual analyses. Without independent information, the relative contribution or effects of source and medium on the observed wave field properties are difficult to quantify. As discussed in section 3.2, in-situ measurements of the depth dependent velocity structure constitute valuable data for the purpose of travel time validation. But the sampled window is too small to allow conclusions about scattering properties at length scales that are relevant for the frequency range considered. Relying thus on wave field properties, we find stabilized earthquake coda and noise kinetic energy ratios at 1 km depth, at albeit different levels. It has been shown that stable coda ratios are independent of the earthquake source and consequently associated with a diffusion process approaching equipartition [*Shapiro et al.*, 2000; *Hennino et al.*, 2001; *Campillo and Paul*, 2003; *Paul et al.*, 2005; *Campillo*, 2006; *Margerin et al.*, 2009]. Diffusive processes may strongly underestimate anisotropic energy fluxes, i.e., isotropy is an asymptotic prediction of the diffusion equation for finite times [*Paul et al.*, 2005; *Campillo*, 2006]. Anisotropy as a result of a narrow source distribution together with equilibrated diffusivity markers are hence not contradictory.

[77] Stabilization of earthquake coda and noise H^2/V^2-ratios at values that exceed theoretical predictions associated with equipartition suggests an excess absorption of *P*-wave energy if the medium is parametrized by a homogeneous half-space [*Margerin et al.*, 2009]. However, in the present context the layered structure more likely controls variable ratios at different frequencies and depths [*Nakahara and Margerin*, 2011]. In contrast to scattering that controls the coda wave field, the stabilized noise-H^2/V^2 ratio can also be explained by a constant source process. This interpretation is supported by the consistently different coda and noise ratios at depth. Generally, cultural noise consists of excess *P*- compared to *S*-wave energy, but *P*-to-*S* scattering dominates. A smaller noise-H^2/V^2 ratio compared to the reference coda ratios are compatible with this view and suggests: Constantly excited noise superimposes the existing weaker scattered wave field component. The constituents of

the scattered noise wave field never equilibrate to the equipartition-level indicated by the coda ratio.

[78] Beamforming results (section 3.3) support this concept. That is, the solutions indicate a predominant ballistic component associated with an upward propagation direction of coherent energy, consistent with a surface generated, refracted trajectory. The increased similarity at higher frequencies between the first two eigenvectors in the adaptive beamforming indicates an increased difficulty to parametrize and interpret a more complex wave propagation situation using a simple model. This can be associated with a frequency dependent isotropy of the source distribution. Or randomized, scattered wave field components become increasingly important. Results of the correlation-based polarization analysis (section 4.1) support the latter interpretation. That is, broadened distributions of directional estimates from individual correlations across the array indicate a controlling effect of the medium. Hence, at this point of the analysis, we have two observations of a frequency dependent degree of the isotropy of propagation directions, and two markers—stabilized earthquake coda ratios and increased scatter in C^1-based direction estimates—that suggest a relevant medium over source effects, respectively.

[79] Additional evidence in favor of the role of scattering comes from the analysis of noise correlation functions, C^1 and C^3 (sections 4 and 5). Importantly, the correlation procedure separates the ballistic from the diffusive, i.e., scattered, wave field components. The very existence of correlation coda waves proves the scattering properties of the medium; we have seen that the C^1 main arrival—controlled by the anisotropic noise wave field—is only a poor approximation of the impulse response. The C^1 coda wave field is more isotropic, demonstrating that coda waves are better linked to the scattering properties of the medium, while the original noise field is more influenced by source effects. The progressive equilibration of C^1 and C^3 coda wave fields highlights the efficiency of multiple scattering in eliminating directivity effects. Nevertheless, asymmetric C^1 coda arrivals indicate the asymptotic nature of this mechanism in the limit of long lapse times.

[80] The constant ratio $\Delta f/f_c$ for the four frequency bands suggests that C^1 SNR levels are controlled by the frequency dependent noise intensity arriving at the borehole array. Because of shorter correlation times, and only four virtual sources, C^3 SNR levels are consistently lower compared to C^1 SNR estimates. Yet they are—in view of these limitations—still surprisingly large, encouraging the utility of C^3 functions in future monitoring efforts. The direct arrival pattern of C^1, C^{3-} and C^{3+} functions allows estimates of seismic velocities across the downhole array. We find that the analysis is hampered by small sensor distances compared to the considered wavelengths. Moreover, the C^{3-} and C^{3+} estimates are biased by the limited and anisotropic virtual source distribution. Considering more separate sensors only, the estimated speeds are generally consistent with the in-situ seismic velocity pattern.

[81] How, then, can we integrate the above discussion and characterize the propagation regime of the high-frequency ambient noise wave field? Summing up, evidence for the ballistic propagation regime is provided by the relatively good match of the data to an incident plane wave model, the highly polarized direct arrival of C^1 functions, and the asymmetric arrival shape. Evidence for the contribution from scattering comes from the stabilized earthquake coda energy ratio, with certain reserves the frequency dependent randomization of propagation directions, and C^1 and C^3 coda waves. We conclude that the ballistic and (multiple) scattered regime coexist. Similar to laboratory results by *Larose et al.* [2007], the first regime dominates the records; the second is weaker but not negligible. Considering the similarity of the H^2/V^2-marker at the borehole and the 40 km distant surface station, we take the view that the dominance is associated with the proximity of the recording site to the excitation location. Anthropogenic activity constantly feeds the open system with (predominantly) longitudinally polarized noise. At the TCDP, the field is not equilibrated but still dominated by the source signature.

[82] Consequently, the wave field is not equipartitioned, and the resulting C^1 correlation functions are only approximations of the impulse response. However, with respect to future monitoring efforts that utilize the high-frequency ambient noise field at depth, we conclude that C^1 functions exhibit the requested stability [*Hadziioannou et al.*, 2009]. The SNR evolution suggests a convergence after about 20 hours and hence a daily resolution at lower frequencies. Frequencies around 3 Hz are most suitable for monitoring studies based on a high wave field coherence across the array and the characteristics of the instrumentation. We think that in addition to techniques that minimize remnant fluctuations in C^1 coda [*Baig et al.*, 2009; *Hadziioannou et al.*, 2011; *Stehly et al.*, 2011], C^3-based monitoring can complement C^1 observations.

Appendix A: Kinetic Energy Ratio, H^2/V^2

[83] To compare noise- and earthquake coda-H^2/V^2 ratios we select 35 $M_l > 5$ earthquakes (8–172 km depth) from a regional catalog. We remove the instrument response from the corresponding 3-component records from the six borehole sensors and from one surface broadband station sampled at 200, 100 sps, respectively. Data are detrended, demeaned, and decimated to 40 and 50 sps, respectively, and bandpass filtered in the four frequency bands centered at $f_c = 1.5$, 3, 6, and 12 Hz, with bandwidths $\Delta f = 1$, 2, 4, 8 Hz.

[84] Noise is analyzed in a 5 min window ending 10 s before the *P*-wave arrival. To determine the coda window, we first take the mean absolute value of the six Z recordings, and the respective absolute value of the surface sensor. The envelope is smoothed with a $\Delta t = 6$ s moving average filter (ma). The coda window begins 20 s after the maximum, and ends when the envelope reaches 10 times the median of the pre-*P* smoothed noise envelope, while the total length is restricted to 150 s. (We note that the stabilization of the marker-ratio in *Shapiro et al.* [2000] and *Hennino et al.* [2001] was interpreted to actually define the coda time window. Our choice is compatible with this idea, i.e., ratios of the examined earthquake codas are equilibrated over the implemented time interval.)

[85] Signals from the two windows are squared, $H^2 = N^2 + E^2$, $V^2 = Z^2$ and smoothed with a Δt ma separated by dt seconds, the inverse of the upper limit of the frequency band. *Shapiro et al.* [2000] and *Hennino et al.* [2001] estimated $\Delta t = 16$, 15 s, respectively, for 1–3 Hz bandpass filtered regional earthquake data from Mexico, where this "[…] window width has been selected to be of the order of the mean free time" [*Shapiro et al.*, 2000]. Then, fluctuations around the

mean value scale with $(\Delta t \Delta f)^{-1/2}$, where Δf is the bandwidth [*Hennino et al.*, 2001].

[86] The (scattering) mean free time t is obtained by determination of the mean free path l, divided by shear wave speed. As noted by *Campillo* [2006], estimates of t and l are difficult to obtain and "[…] ambiguous in most cases since both scattering and dissipation may contribute to the decay of a propagating wave." Estimates for l (for 1–10 Hz) in the Mexican crust in *Shapiro et al.* [2000] and *Hennino et al.* [2001] were obtained by *Margerin et al.* [1999] using numerical simulations of Radiative Transfer Theory, concluding that l is of the order of the crustal thickness. Lacking independent estimates on possibly frequency dependent l, we use Δt = 15 s for the whole frequency range 1–16 Hz. Possible systematic frequency dependent variations in the level of fluctuations are therefore related to the bandwidth.

Appendix B: Beamforming

[87] We perform plane wave beamforming on three components individually. Two beamformer outputs are computed, the 'conventional', b_c, and 'minimum-variance' or 'adaptive', b_a, estimate. For both estimates, 1-hour segments of instrument response removed continuous data are detrended, demeaned, and whitened to reduce effects of transients. Here, we use our common central frequencies f_c = 1.5, 3, 6, 12 Hz, but we apply more narrow bandwidths Δf = 0.25, 0.5, 1, 2 Hz.

[88] For the conventional estimate [*Capon*, 1969], the Fourier transform is computed at 50 linearly spaced frequencies ω in each frequency band associated with ω_c, resulting in a complex-valued vector $\mathbf{x}(\omega)$, with $\omega = 2\pi f$. The cross spectral density matrix $\mathbf{C}(\omega)$ is given by $\mathbf{x}(\omega)\mathbf{x}^*(\omega)$, with '*' denoting the complex conjugate transpose. The plane wave response for the array as a function of incidence angle, ϕ—classically measured with respect to vertical, down—, and phase velocity, c, is given by $\mathbf{p}(\omega, s) = \exp(i\omega \mathbf{r} s)$, where $s = \cos(\phi)/c$ is vertical slowness, and $\mathbf{r}$ denotes sensor depths relative to the average array depth. The power associated with a beam, i.e., the (1-hour) beamformer output averaged over the narrow band centered on frequency ω_c is then given by $b_c(\omega_c, s) = \langle\, \mathbf{p}^* \mathbf{C}\, \mathbf{p} \,\rangle / N$. The number of sensors is given by N, and $\langle \cdot \rangle$ indicates frequency averaging. Recall that the maximum signal gain, i.e., the maximum beamformer output, is obtained by the $\mathbf{p}$ vector that simply removes the propagation induced phase shifts [*Wagner and Owens*, 1996].

[89] The minimum variance or adaptive estimate enhances the resolution compared to the conventional estimate; Moreover, applying a singular value decomposition to the cross spectral density matrix, the method is able to identify several simultaneously acting sources with variable strength. However, this comes at the cost of an increased sensitivity to speed mismatches [*Debever and Kuperman*, 2007; *Vandemeulebrouck et al.*, 2009]. For the adaptive estimate, we split 1-hour data up into H segments. The cross spectral density matrix is then written as $\mathbf{C}(\omega) = \varepsilon[\mathbf{x}(\omega)\mathbf{x}^*(\omega)]$, where $\varepsilon[\cdot]$ denotes the temporal mean over the H segments, resulting in a full-rank matrix $\mathbf{C}(\omega)$. Considering the full matrix $\mathbf{C}$, the adaptive beam power is given by $b_a(\omega_c, s) = \left\langle \left[\mathbf{p}^* \mathbf{C}^{-1} \mathbf{p}\right]^{-1} \right\rangle$. Applying singular value decomposition, $\mathbf{C}$ is decomposed into matrices $\widetilde{\mathbf{C}}_{k_n}$ that correspond to one of the up to $n = 1, \ldots, N$ (number of sensors) eigenvalues. Power associated with multiple sources is associated with significantly different, non-zero eigenvalues. The beamformer output is given by $b_a(\omega_c, s) = \left\langle \left[\mathbf{p}^* \widetilde{\mathbf{C}}_{k_n}^{-1} \mathbf{p}\right]^{-1} \right\rangle$. In the notation used in Figures 5b–5d, $b_a(k_0)$ corresponds to the adaptive output associated with no decomposition, and $b_a(k_1)$ and $b_a(k_2)$ correspond to solutions associated with the largest and second largest eigenvalues, respectively.

Appendix C: Cross Correlation of Ambient Noise (C^1)

[90] Correlation preprocessing includes removal of the instrument response from continuously recorded 3-component data sampled at 200 Hz, detrending, demeaning, and down sampling. (For illustrative and peak-arrival picking (section 4.3) purposes, we decrease the new sampling rate only by a factor of two.) Whitening in the four frequency bands f_c = 1.5, 3, 6, 12 Hz, Δf = 1, 2, 4, 8 Hz is routinely applied, except for the polarization analysis, where relative amplitude information is essential [*Landès et al.*, 2010]. Throughout this work, C^1 functions are hourly computed. In all cases, we apply amplitude clipping at three times the standard deviation of hourly amplitude distributions. We chose hourly over daily segmentation to utilize more data in case of intermittent recording problems. No difference was found between 24-hour correlations, and stacks of 24 1-hour correlations for complete 24-hour recordings. Significant differences due to variable amplitude statistics arise only when the segment duration is shorter than 30 minutes. Throughout section 4 stacks are constructed in an iterative process, using individual 1-hour C^1 functions from 15 days in February 2009 that show a high zero-lag correlation coefficient with the resulting stack. This method disregards time windows contaminated by transients or other recording problems. The correlations are scaled by the square root of the total signal energy recorded at the two sensors. Thus, the maximum of the C^1 function corresponds to the coherence level between the two stations.

Appendix D: Polarization Analysis Based on C^1 Functions

[91] *Landès et al.* [2010] demonstrated that, in the case of plane P-waves "the covariance matrix for the three component record at a single station and the covariance matrix for the cross correlations between two stations differ only by a scalar factor. Therefore, the eigenvectors of these matrices are the same which proves the polarization analysis can be performed either on cross correlation or on 3-component records." We compute the 15 inter-sensor ZN-, ZE-, and ZZ-C^1 correlation functions following the steps discussed in Appendix C. Note that the azimuth of the preferential propagation direction of diffuse field energy can be estimated from different amplitudes of 1-component correlations using an array with horizontal geometry [*Larose et al.*, 2005]. Different to the standard normalization applied in Appendix C, however, records are not whitened to preserve amplitude ratios between components in the cross correlation functions [*Landès et al.*, 2010]. We note that *Roux* [2009] performed a similar particle motion analysis that does include whitening

during preprocessing. Empirical observations using synthetic noise suggests that the coherent phase information of the sampled wave field is the dominant factor controlling amplitudes of the correlation functions. Even 1-bit normalized traces yield practically identical correlation amplitude values, provided that the correlated signals contain a sufficient number of periods. See also the related discussion of results by *Cupillard and Capdeville* [2010] and *Cupillard et al.* [2011] by *Prieto et al.* [2011]. Here, data are corrected for instrument response, detrended, demeaned, and filtered in the four frequency bands. Amplitudes are clipped at four times the hourly standard deviation to reduce effects of large amplitude transients [*Landès et al.*, 2010]. As discussed in Appendix C, only records with a high zero-lag similarity to the resulting stack are used.

[92] From the three eigenvectors ($\lambda_0 > \lambda_1 > \lambda_2$) of an individual covariance matrix $\mathbf{C}$, we compute incidence angle, $\cos(\phi) = v_{1ZZ}$, azimuth, $\tan\theta = v_{1ZE}/v_{1ZN}$, and rectilinearity $R = 1 - (\lambda_1 + \lambda_2)/2/\lambda_0$. The applied azimuth determination tunes the analysis to *P*-wave motion; in case of *SH* analysis, $\tan\theta = v_{1ZN}/v_{1ZE}$. Here, $\mathbf{v}_1 = v_{1Z[N,E,Z]}$ denotes the normalized eigenvector corresponding to the largest eigenvalue λ_0 [*Jepsen and Kennett*, 1990]. As a caveat, we note that these directional parameters are calculated from the particle motion of the local wave field. These directions do not necessarily coincide with the direction of propagation [*Jepsen and Kennett*, 1990].

[93] We tested the method analyzing *P*-wave motion of the 35 regional intermediate size earthquakes. The inferred azimuths and incidence angles of individual 3-component data were satisfactorily reproduced by the ZN-, ZE-, and ZZ-correlations of data taken from a 1 s window around the *P*-wave arrival. With respect to the above caveat, we find that back azimuths determined for events northeast and east of the borehole are consistently smaller compared to the actual bearings. Moreover, *P*-wave particle motion of events to the South show values of θ that differ almost 90° from the connecting horizontal direction. The particle motion is, however, compatible with the east-west dipping stratification resulting from the regional tectonic situation. The discrepancy does hence not point to problems in our analysis, but to interesting wave propagation and polarization effects.

Appendix E: Measurement of Phase Velocities Using the Direct Arrival of Correlation Functions

[94] We estimate velocities of the phases that travel across the array—i.e., the propagation speed of the correlation direct arrival—applying two methods to each of the six ZZ-, EE-, and NN-C^1 and -$\partial_\tau C^1$ functions (section 4.3), and to the ZZ-C^3 and -$\partial_\tau C^3$ functions (section 5.2). First, we find the maximum of each inter-sensor C^1, $\partial_\tau C^1$ function, and subtract the corresponding time lag of the associated autocorrelation peaks, which simplifies to $\tau = 0$ for C^1 autocorrelations. Second, we determine the relative lag that maximizes the correlation between a C^1, $\partial_\tau C^1$ function and the associated autocorrelation. For example, we determine the lag that maximizes the correlation of the $\partial_\tau C^1$ function associated with the correlation pair BHS1-BHS4 with the derivative of the BHS1 C^1 autocorrelation. The inter-sensor velocity pattern obtained with the four methods are consistent and do not show systematic deviations. Throughout this work, we discuss values obtained from the correlation technique applied to the $\partial_\tau C^{1,3}$ functions (Table 1).

[95] We note that it is not clear how the asymmetric energy distribution discussed in the text controls the shape of the arrival, i.e., how positive and negative lag pulses interfere, distorting the direct arrival pulse and therefore biasing the measurements. While numerical simulations are assumed to clarify this issue, systematic numerical experiments are beyond the scope of this paper.

Appendix F: Correlation of C^1 Coda (C^3)

[96] Construction of the C^3 function, i.e., the correlation of the coda of the C^1 function, follows the method discussed by *Stehly et al.* [2008] and *Froment et al.* [2011]. The analysis is limited to the ZZ-C^3 function. Processing consists of the following steps.

[97] 1. Cross correlations (C^1) between all sensor pairs in a given frequency band are computed following Appendix C. The choice of the stacking interval of individual 1-hour C^1 functions is discussed in section 5. While an iterative stacking procedure is applied in Section 4.2, the C^3 convergence analysis (section 5.1) does not utilize such a signal optimization strategy, resulting in larger temporal fluctuations.

[98] 2. To construct the C^3 function between two sensors *A* and *B* from a *N*-sensor network, a third sensor, *S*, is chosen playing the role of a 'virtual source.'

[99] 3. We select a coda wave time window t_3 in the *A*-*S* and *B*-*S* C^1 functions, respectively, limited between $\tau = [20\ m] \times T_c$, with $100 < m < 300$ (section 5), and T_c the central period of the frequency band. C^1 coda at negative and positive correlation lags (C^{1-}, C^{1+}) is processed individually. Neglecting waves around $\tau = 0$ reduces the influence of ballistic contributions, therefore selecting only scattered waves for recorrelation.

[100] 4. Selected C^{1-}, C^{1+} codas are whitened in each frequency band and cross correlated between *A*-*S* and *B*-*S*, yielding the two functions, $C_S^{3-}(\tau')$, $C_S^{3+}(\tau')$. For C_S^{3-}, C^{1-} codas are time reversed before correlation. (Depending on the order in which C^1 functions are constructed between all sensor pairs—potentially yielding the *S*-*A* C^1 function in case $A < S$, with '<' indicating processing order—C^1 functions have to be time reversed to maintain the 'direction' of correlation.)

[101] 5. For sensor pair *A*, *B*, steps 2–4 are repeated for each of the remaining $n = N - 2$ virtual sources, i.e., all *n* stations become *S*; the resulting functions are stacked to obtain C^{3-} and C^{3+}. Note that *Stehly et al.* [2008] also considered correlation pairs between negative and positive C^1 coda lags in the stacking process eventually leading to C^3. However, their contributions to the targeted reconstruction of the Green's function were regarded as insignificant due to very low SNR, and their computation omitted thereafter [*Froment et al.*, 2011].

[102] 6. The average of C^{3-} and C^{3+} finally constitutes the $C^3(x_A, x_B, \tau')$ function between *A* and *B*.

[103] In the present case, individual C^{3-}, C^{3+} functions have a prime importance in the assessment of the ballistic arrival between two sensors around $\tau' = 0$, as discussed in section 5.

[104] **Acknowledgments.** The authors acknowledge reviews from L. Margerin, an anonymous reviewer, and the Associated Editor, which helped to improve the manuscript. We thank the Institute of Earth Sciences, Academia Sinica, Taiwan, for providing broadband data from the TDCB station. We thank E. Larose and B. Froment for useful discussions. This work was supported by the European Research Council (Advanced grant Whisper L27507), and by the National Science Council, Taiwan (NSC 98-2116-M-008-007). Some figures were made using GMT [*Wessel and Smith*, 1991].

References

Abercrombie, R. E. (1995), Earthquake source scaling relationships from −1 to 5 *M*L using seismograms recorded at 2.5 km depth, *J. Geophys. Res.*, *100*(B12), 24,015–24,036.

Aki, K., and P. G. Richards (Eds.) (1980), *Quantitative Seismology*, 1st ed., 932 pp., W. H. Freeman, San Francisco, Calif.

Atef, A. H., K. H. Liu, and S. S. Gao (2009), Apparent weekly and daily earthquake periodicities in the western United States, *Bull. Seismol. Soc. Am.*, *99*(4), 2273–2279, doi:10.1785/0120080217.

Baig, A. M., M. Campillo, and F. Brenguier (2009), Denoising seismic noise correlations, *J. Geophys. Res.*, *114*, B08310, doi:10.1029/2008JB006085.

Ben-Zion, Y. (2008), Collective behavior of earthquakes and faults: Continuum-discrete transitions, progressive evolutionary changes and different dynamic regimes, *Rev. Geophys.*, *46*, RG4006, doi:10.1029/2008RG000260.

Ben-Zion, Y., and P. Leary (1986), Thermoelastic strain in a half space covered by unconsolidated material, *Bull. Seismol. Soc. Am.*, *76*(5), 1447–1460.

Berger, J. (1975), A note on thermoelastic strains and tilts, *J. Geophys. Res.*, *80*(2), 274–277.

Bohnhoff, M., and M. D. Zoback (2010), Oscillation of fluid-filled cracks triggered by degassing of CO_2 due to leakage along wellbores, *J. Geophys. Res.*, *115*, B11305, doi:10.1029/2010JB000848.

Brenguier, F., M. Campillo, C. Hadziioannou, N. M. Shapiro, R. M. Nadeau, and E. Larose (2008), Postseismic relaxation along the San Andreas Fault at Parkfield from continuous seismological observations, *Science*, *321*, 1478–1481, doi:10.1126/science.1160943.

Burtin, A., L. Bollinger, J. Vergne, R. Cattin, and J. L. Nábělek (2008), Spectral analysis of seismic noise induced by rivers: A new tool to monitor spatiotemporal changes in stream hydrodynamics, *J. Geophys. Res.*, *113*, B05301, doi:10.1029/2007JB005034.

Campillo, M. (2006), Phase and correlation of 'random' seismic fields and the reconstruction of the Green function, *Pure Appl. Geophys.*, *163*, 475–502, doi:10.1007/s00024-005-0032-8.

Campillo, M., and A. Paul (2003), Long-range correlations in the diffuse seismic coda, *Science*, *299*, 547–549, doi:10.1126/science.1078551.

Capon, J. (1969), High-resolution frequency-wavenumber spectrum Analysis, *Proc. IEEE*, *57*(8), 1408–1418.

Chavarria, J. A., P. E. Malin, and E. Shalev (2004), The SAFOD Pilot Hole seismic array: Wave propagation effects as a function of sensor depth and source location, *Geophys. Res. Lett.*, *31*, L12S07, doi:10.1029/2003GL019382.

Chen, J. H., B. Froment, Q. Y. Liu, and M. Campillo (2010), Distribution of seismic wave speed changes associated with the 12 May 2008 Mw 7.9 Wenchuan earthquake, *Geophys. Res. Lett.*, *37*, L18302, doi:10.1029/2010GL044582.

Chouet, B. (1988), Resonance of a fluid-driven crack: Radiation properties and implications for the source of long period events and harmonic tremor, *J. Geophys. Res.*, *93*(B5), 4375–4400.

Courtland, R. (2008), Harnessing the hum, *Nature*, *453*, 146–148.

Cupillard, P., and Y. Capdeville (2010), On the amplitude of surface waves obtained by noise correlation and the capability to recover the attenuation: a numerical approach, *Geophys. J. Int.*, *181*, 1687–1700, doi:10.1111/j.1365-246X.2010.04568.x.

Cupillard, P., L. Stehly, and B. Romanowicz (2011), The one-bit noise correlation: A theory based on the concepts of coherent and incoherent noise, *Geophys. J. Int.*, *184*, 1397–1414, doi:10.1111/j.1365-246X.2010.04923.x.

Debever, C., and W. A. Kuperman (2007), Robust matched-filter processing using a coherent broadband white noise constraint processor, *J. Acoust. Soc. Am.*, *122*(4), 1979–1986, doi:10.1121/1.2769830.

Doan, M. L., E. E. Brodsky, Y. Kano, and K. F. Ma (2006), In situ measurement of the hydraulic diffusivity of the active Chelungpu Fault, Taiwan, *Geophys. Res. Lett.*, *33*, L16317, doi:10.1029/2006GL026889.

Ferrazzini, V., and K. Aki (1987), Slow waves trapped in a fluid-filled infinite crack: Implication for volcanic tremor, *J. Geophys. Res.*, *92*(B9), 9215–9223.

Frankel, A., and R. W. Clayton (1986), Finite difference simulations of seismic scattering: Implications for the propagation of short-period waves in the crust and models of crustal heterogeneity, *J. Geophys. Res.*, *91*(B6), 6465–6489.

Froment, B., M. Campillo, P. Roux, P. Gouédard, A. Verdel, and R. L. Weaver (2010), Estimation of the effect of nonisotropically distributed energy on the apparent arrival time in correlations, *Geophysics*, *75*(5), 85–93, doi:10.1190/1.3483102.

Froment, B., M. Campillo, and P. Roux (2011), Reconstructing the Green's function through iteration of correlations, *C. R. Geosci.*, *343*, 623–632, doi:10.1016/j.crte.2011.03.001.

Gouédard, P., P. Roux, M. Campillo, and A. Verdel (2008), Convergence of the two-point correlation function toward the Green's function in the context of a seismic-prospecting data set, *Geophysics*, *73*(6), 47–53, doi:10.1190/1.2985822.

Gurrola, H., J. B. Minster, H. Given, F. Vernon, J. Berger, and R. Aster (1990), Analysis of high-frequency seismic noise in the western United States and eastern Kazakhstan, *Bull. Seismol. Soc. Am.*, *80*(4), 951–970.

Hadziioannou, C., E. Larose, O. Coutant, P. Roux, and M. Campillo (2009), Stability of monitoring weak changes in multiply scattering media with ambient noise correlations: Laboratory experiments, *J. Acoust. Soc. Am.*, *125*(6), 3688–3695, doi:10.1121/1.3125345.

Hadziioannou, C., E. Larose, A. Baig, P. Roux, and M. Campillo (2011), Improving temporal resolution in ambient noise monitoring of seismic wave speed, *J. Geophys. Res.*, *116*, B07304, doi:10.1029/2011JB008200.

Hennino, R., N. Trégourès, N. M. Shapiro, L. Margerin, M. Campillo, B. A. van Tiggelen, and R. L. Weaver (2001), Observation of equipartitioning of seismic waves, *Phys. Rev. Lett.*, *86*(15), 3447–3450, doi:10.1103/PhysRevLett.86.3447.

Hillers, G., and Y. Ben-Zion (2011), Seasonal variations of observed noise amplitudes at 2–18 Hz in southern California, *Geophys. J. Int.*, *184*, 860–868, doi:10.1111/j.1365-246X.2010.04886.x.

Hirono, T., et al. (2007), Nondestructive continuous physical property measurements of core samples recovered from hole B, Taiwan Chelungpu-Fault Drilling Project, *J. Geophys. Res.*, *112*, B07404, doi:10.1029/2006JB004738.

Jepsen, D. C., and B. L. N. Kennett (1990), Three-component analysis of regional seismograms, *Bull. Seismol. Soc. Am.*, *80*(6), 2032–2052.

Koch, K., and K. Stammler (2003), Detection and elimination of time synchronization problems for the GERESS array by correlating microseismic noise, *Seismol. Res. Lett.*, *74*(6), 803–816.

Konno, K., and T. Ohmachi (1998), Ground-motion characteristic estimated from spectral ratio between horizontal and vertical components of microtremor, *Bull. Seismol. Soc. Am.*, *88*, 228–241.

Koper, K. D., B. de Foy, and H. Benz (2009), Composition and variation of noise recorded at the Yellowknife Seismic Array, 1991–2007, *J. Geophys. Res.*, *114*, B10310, doi:10.1029/2009JB006307.

Landès, M., F. Hubans, N. M. Shapiro, A. Paul, and M. Campillo (2010), Origin of deep ocean microseisms by using teleseismic body waves, *J. Geophys. Res.*, *115*, B05302, doi:10.1029/2009JB006918.

Larose, E., A. Khan, Y. Nakamura, and M. Campillo (2005), Lunar subsurface investigated from correlation of seismic noise, *Geophys. Res. Lett.*, *33*, L16201, doi:10.1029/2005GL023518.

Larose, E., P. Roux, and M. Campillo (2007), Reconstruction of Rayleigh-Lamb dispersion spectrum based on noise obtained from an air-jet forcing, *J. Acoust. Soc. Am.*, *122*(6), 3437–3444, doi:10.1121/1.2799913.

Larose, E., P. Roux, M. Campillo, and A. Derode (2008), Fluctuations of correlations and Green's function reconstruction: Role of scattering, *J. Appl. Phys.*, *103*, 114907, doi:10.1063/1.2939267.

Lewis, M. A., and P. Gerstoft (2012), Shear wave anisotropy from cross-correlation of seismic noise in the Parkfield pilot hole, *Geophys. J. Int.*, *188*, 626–630, doi:10.1111/j.1365-246X.2011.05285.x.

Lin, Y.-Y., K.-F. Ma, and V. Oye (2012), Observation and scaling of microearthquakes from TCDP borehole seismometers, *Geophys. J. Int.*, in press.

Lobkis, O. I., and R. L. Weaver (2001), On the emergence of the Green's function in the correlations of a diffuse field, *J. Acoust. Soc. Am.*, *110*(6), 3001–3017.

Ma, K.-F., et al. (2006), Slip zone and energetics of a large earthquake from the Taiwan Chelungpu-fault Drilling Project, *Nature*, *444*, 473–476, doi:10.1038/nature05253.

Ma, S., R. J. Archuleta, and M. T. Page (2007), Effects of large-scale topography on ground motions, as demonstrated by a study of the San Gabriel Mountains, Los Angeles, California, *Bull. Seismol. Soc. Am.*, *97*(6), 2066–2079, doi:10.1785/0120070040.

Malin, P., E. Shalev, H. Balven, and C. Lewis-Kenedi (2006), Structure of the San Andreas Fault at SAFOD from P-wave tomography and fault-guided wave mapping, *Geophys. Res. Lett.*, *33*, L13314, doi:10.1029/2006GL025973.

Margerin, L., M. Campillo, and B. van Tiggelen (1998), Radiative transfer and diffusion of waves in a layered medium: New insight into coda *Q*, *Geophys. J. Int.*, *134*, 569–612.

Margerin, L., M. Campillo, N. M. Shapiro, and B. van Tiggelen (1999), Residence time of diffuse waves in the crust as a physical interpretation of coda *Q*: Application to seismograms recorded in Mexico, *Geophys. J. Int.*, *138*, 343–352.

Margerin, L., B. A. van Tiggelen, and M. Campillo (2001), Effect of absorption on energy partition of elastic waves in the seismic coda, *Bull. Seismol. Soc. Am.*, *91*(3), 624–627.

Margerin, L., M. Campillo, B. A. van Tiggelen, and R. Hennino (2009), Energy partition of seismic coda waves in layered media: theory and application to Pinyon Flats Observatory, *Geophys. J. Int.*, *177*, 571–585, doi:10.1111/j.1365-246X.2008.04068.x.

McNamara, D. E., and R. P. Buland (2004), Ambient noise levels in the continental United States, *Bull. Seismol. Soc. Am.*, *94*(4), 1517–1527.

Meier, U., N. M. Shapiro, and F. Brenguier (2010), Detecting seasonal variations in seismic velocities within Los Angeles basin from correlations of ambient seismic noise, *Geophys. J. Int.*, *181*, 985–996, doi:10.1111/j.1365-246X.2010.04550.x.

Nakahara, H., and L. Margerin (2011), Testing equipartition for *S*-wave coda using borehole records of local earthquakes, *Bull. Seismol. Soc. Am.*, *101*(5), 2243–2251, doi:10.1785/0120100353.

Paul, A., M. Campillo, L. Margerin, E. Larose, and A. Derode (2005), Empirical synthesis of time-asymmetrical Green function from the correlation of coda waves, *J. Geophys. Res.*, *110*, B08302, doi:10.1029/2004JB003521.

Poupinet, G., W. Ellsworth, and J. Frechet (1984), Monitoring velocity variations in the crust using earthquake doublets: An application to the Calaveras Fault, California, *J. Geophys. Res.*, *89*(B7), 5719–5731.

Prieto, G. A., M. Denolle, J. F. Lawrence, and G. C. Beroza (2011), On amplitude information carried by the ambient seismic field, *C. R. Geosci.*, *343*, 600–614, doi:10.1016/j.crte.2011.03.001.

Ringdal, F., and H. Bungum (1977), Noise level variation at NORSAR and its effect on detectability, *Bull. Seismol. Soc. Am.*, *67*(2), 479–492.

Rivet, D., M. Campillo, N. M. Shapiro, V. Cruz-Atienza, M. Radiguet, N. Cotte, and V. Kostoglodov (2011), Seismic evidence of nonlinear crustal deformation during a large slow slip event in Mexico, *Geophys. Res. Lett.*, *38*, L08308, doi:10.1029/2011GL047151.

Rost, S., and C. Thomas (2002), Array seismology: Methods and applications, *Rev. Geophys.*, *40*(3), 1008, doi:10.1029/2000RG000100.

Roux, P. (2009), Passive seismic imaging with direct ambient noise: Application to surface waves and the San Andreas Fault in Parkfield, CA, *Geophys. J. Int.*, *179*, 367–373, doi:10.1111/j.1365-246X.2009.04282.x.

Roux, P., K. G. Sabra, P. Gerstoft, W. A. Kuperman, and M. C. Fehler (2005), P-waves from cross-correlation of seismic noise, *Geophys. Res. Lett.*, *32*, L19303, doi:10.1029/2005GL023803.

Sabra, K. G., P. Gerstoft, P. Roux, W. A. Kuperman, and M. C. Fehler (2005a), Extracting time-domain Green's function estimates from ambient seismic noise, *Geophys. Res. Lett.*, *32*, L03310, doi:10.1029/2004GL021862.

Sabra, K. G., P. Roux, and W. A. Kuperman (2005b), Emergence rate of the time-domain Green's function from the ambient noise cross-correlation function, *J. Acoust. Soc. Am.*, *118*(6), 3524–3531, doi:10.1121/1.2109059.

Sánchez-Sesma, F. J., et al. (2011), A theory for microtremor *h*/*v* spectral ratio: application for a layered medium, *Geophys. J. Int.*, *186*, 221–225, doi:10.1111/j.1365-246X.2011.05064.x.

Sens-Schönfelder, C., and U. Wegler (2006), Passive image interferometry and seasonal variations of seismic velocities at Merapi Volcano, Indonesia, *Geophys. Res. Lett.*, *33*, L21302, doi:10.1029/2006GL027797.

Shapiro, N. M., M. Campillo, L. Margerin, S. K. Singh, V. Kostoglodov, and J. Pacheco (2000), The energy partitioning and the diffuse character of the seismic coda, *Bull. Seismol. Soc. Am.*, *90*(3), 655–665.

Shapiro, N. M., M. Campillo, L. Stehly, and M. H. Ritzwoller (2005), High-resolution surface-wave tomography from ambient seismic noise, *Science*, *307*, 1615–1618, doi:10.1126/science.1108339.

Stehly, L., M. Campillo, and N. M. Shapiro (2006), A study for the seismic noise from its long-range correlation properties, *J. Geophys. Res.*, *111*, B10306, doi:10.1029/2005JB004237.

Stehly, L., M. Campillo, B. Froment, and R. L. Weaver (2008), Reconstructing Green's function by correlation of the coda of the correlation (c^3) of ambient seismic noise, *J. Geophys. Res.*, *113*, B11306, doi:10.1029/2008JB005693.

Stehly, L., P. Cupillard, and B. Romanowicz (2011), Towards improving ambient noise tomography using simultaneously curvelet denoising filters and SEM simulations of seismic ambient noise, *C. R. Geosci.*, *343*, 591–599, doi:10.1016/j.crte.2011.03.005.

Vandemeulebrouck, J., R. Roux, P. Gouédard, A. Legaz, A. Revil, A. W. Hurst, A. Bolève, and A. Jardani (2009), Application of acoustic noise and self-potential localization techniques to a buried hydrothermal vent (Waimangu Old Geyser site, New Zealand), *Geophys. J. Int.*, *180*, 883–890, doi:10.1111/j.1365-246X.2009.04454.x.

Wagner, G. S., and T. J. Owens (1996), Signal detection using multichannel seismic data, *Bull. Seismol. Soc. Am.*, *86*(1A), 221–231.

Wang, Y.-J., K.-F. Ma, F. Mouthereau, and D. Eberhart-Phillips (2010), Three-dimensional *Qp*- and *Qs*-tomography beneath Taiwan orogenic belt: Implications for tectonic and thermal structure, *Geophys. J. Int.*, *180*, 891–910, doi:10.1111/j.1365-246X.2009.04459.x.

Wang, Y.-J., Y.-Y. Lin, K.-F. Ma, and M.-C. Lee (2012), Fault Zone *Q* structure discovered from the Taiwan Chelungpu Fault Borehole Seismometer array (TCDPBHS), *Tectonophysics*, doi:10.1016/j.tecto.2011.12.027, in press.

Weaver, R. L. (1982), On diffuse waves in solid media, *J. Acoust. Soc. Am.*, *71*(6), 1608–1609.

Weaver, R. L. (2011), On the amplitudes of correlations and the inference of attenuations, specific intensities and site factors from ambient noise, *C. R. Geosci.*, *343*, 615–622, doi:10.1016/j.crte.2011.07.001.

Weaver, R. L., and O. I. Lobkis (2005), Fluctuations in diffuse field-field correlations and the emergence of the Green's function in open systems, *J. Acoust. Soc. Am.*, *117*(6), 3432–3439, doi:10.1121/1.1898683.

Weaver, R. L., B. Froment, and M. Campillo (2009), On the correlation of non-isotropically distributed ballistic scalar diffuse waves, *J. Acoust. Soc. Am.*, *126*(4), 1817–1826, doi:10.1121/1.3203359.

Wegler, U., and C. Sens-Schönfelder (2007), Fault zone monitoring with passive image interferometry, *Geophys. J. Int.*, *168*, 1029–1033, doi:10.1111/j.1365-246X.2006.03284.

Wessel, P., and W. H. F. Smith (1991), Free software helps map and display data, *Eos Trans. AGU*, *72*(41), 441, doi:10.1029/90EO00319.

Withers, M. M., R. C. A. Young, C. J. Young, and E. P. Chael (1996), High-frequency analysis of seismic background noise as a function of wind speed and shallow depth, *Bull. Seismol. Soc. Am.*, *86*(5), 1507–1515.

Wu, H.-Y., K.-F. Ma, M. Zoback, N. Boness, H. Ito, J.-H. Hung, and S. Hickman (2007), Stress orientation of Taiwan Chelungpu-Fault Drilling Project (TCDP) hole-A as observed from geophysical logs, *Geophys. Res. Lett.*, *34*, L01303, doi:10.1029/2006GL028050.

Young, C. J., E. P. Chael, M. M. Withers, and R. C. Aster (1996), A comparison of the high-frequency (>1 Hz) surface and subsurface noise environment at three sites in the United States, *Bull. Seismol. Soc. Am.*, *86*(5), 1516–1528.

Zoback, M., S. Hickman, W. Ellsworth, and the SAFOD Science Team (2011), Scientific drilling into the San Andreas Fault Zone—An overview of SAFOD's first five years, *Sci. Drill.*, *11*, 14–28, doi:10.2204/iodp.sd.11.02.2011.